Effect of compressibility on the small-scale structures in hypersonic turbulent boundary layer ⊘

Dehao Xu (许得豪) ✉; Jianchun Wang (王建春); Changping Yu (于长平); ... et. al

Check for updates
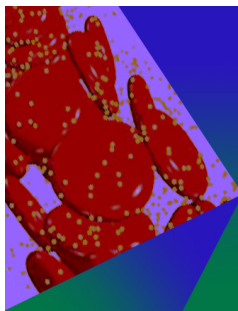
View Online   Export Citation   CrossMark

Articles You May Be Interested In

Contribution of flow topology to the kinetic energy flux in hypersonic turbulent boundary layer

Physics of Fluids (April 2022)

Physics of Fluids

Special Topic: Flow and Forensics

Submit Today!

Effect of compressibility on the small-scale structures in hypersonic turbulent boundary layer

View Online Export Citation CrossMark

Dehao Xu (许得豪),[1,a] 🆔 Jianchun Wang (王建春),[2,b] 🆔 Changping Yu (于长平),[3] Xinliang Li (李新亮),[3] 🆔
and Shiyi Chen (陈十一)[1,2,c]

AFFILIATIONS

[1]State Key Laboratory of Turbulence and Complex Systems, College of Engineering, Peking University, Beijing 100871,
People's Republic of China
[2]Department of Mechanics and Aerospace Engineering, Southern University of Science and Technology, Shenzhen 518055,
People's Republic of China
[3]Laboratory of High Temperature Gas Dynamics, Institute of Mechanics, Chinese Academy of Sciences, Beijing 100190,
People's Republic of China

[a]Author to whom correspondence should be addressed: xudh@mail.sustech.edu.cn
[b]Electronic mail: wangjc@sustech.edu.cn
[c]Electronic mail: chensy@sustech.edu.cn

ABSTRACT

The effects of the wall temperature and local compressibility on the small-scale structures, local flow topology, and enstrophy production in the hypersonic turbulent boundary layer are numerically investigated. The colder wall temperature significantly enhances the unstable topologies and non-focal topologies near the wall, mainly due to stronger compressibility and more sheet-like structures. The eigenvalue decomposition of the strain rate tensor is introduced to investigate the mechanism of the enstrophy production and small-scale structures. It is shown that in the near wall region, the enstrophy production is mainly governed by the intermediate eigenvalue of strain-rate tensor through flow topologies unstable node/saddle/saddle (UN/S/S), stable focus/stretching (SFS), unstable focus/stretching, and unstable node/unstable node/unstable node, while the enstrophy destruction is primarily contributed by the intermediate eigenvalue through flow topologies stable node/saddle/saddle, stable focus/compressing (SFC), and stable node/stable node/stable node. Moreover, in the far wall region, the third eigenvalue in flow topology SFS and the intermediate eigenvalue in UN/S/S make major contributions to the enstrophy production, while the first eigenvalue in flow topologies unstable focus/compressing and SFC, and the intermediate eigenvalue in SFC mainly lead to the enstrophy destruction.

Published under an exclusive license by AIP Publishing. https://doi.org/10.1063/5.0091731

I. INTRODUCTION

The mechanisms and properties of supersonic and hypersonic turbulent boundary layers are urgent to be investigated due to their importance in aerospace engineering.[1–3] The supersonic and hypersonic turbulent boundary layers are more intricate than the incompressible turbulent boundary layer due to the remarkable compressibility.[4–10] The investigation about the hypersonic turbulent boundary layer with an isothermal wall condition is imperiously demanding due to the outstanding importance of the design of the hypersonic aircrafts. Previous investigations[4,11,12] were mainly concentrated on the average and second-order statistical properties of flow fields, including the van Driest transformation for mean velocity, Walz's relation, Morkovin's scaling, and the strong Reynolds analogy

(SRA). It is necessary to study the statistics and structures of small-scale motions in the hypersonic turbulent boundary layer.

The velocity gradient structures and local flow topology of the small scale motions are related to various turbulent flow processes, including kinetic energy dissipation, enstrophy production, vortex stretching, scalar mixing, material element deformation, and turbulent cascade. The statistics of the velocity gradient tensor and local flow topology in incompressible turbulence has been widely investigated.[13,14] Chong et al.[15] introduced a comprehensive classification of the three-dimensional flow patterns based on the invariants of the velocity gradient tensor. It was noted that in the incompressible turbulence, the first invariant (P) of the velocity gradient tensor is zero due to the continuity condition. Therefore, the local flow patterns were

reduced to be characterized by the two-dimensional plane of the second (Q) and third (R) invariants of the velocity gradient tensor.

Blackburn et al.[16] investigated the flow topologies of the velocity gradient tensor in the incompressible turbulent channel flow and demonstrated that the stable focus/stretching and unstable node/saddle/saddle topologies are preferred in the flow away from the wall. Chong et al.[17] identified a self-similar teardrop shape of the joint PDF of Q and R of the velocity gradient tensor from the buffer layer onward in the incompressible zero-pressure-gradient turbulent boundary layer. Elsinga and Marusic[18] evaluated the average flow pattern and then provided an explanation for the universal teardrop shape of the joint PDF in Q–R plane. Lozano-Durán et al.[19] applied the multiscale analysis on the invariants of the filtered velocity gradient tensor in the logarithmic layer in the incompressible turbulent channel flow. They concluded that the mean shear was the major reason for the absence of self-similarity as the filter width increases in the inertial range. These observations were focused on the incompressible turbulence; however, the mechanisms in compressible turbulence are more complicated than those in incompressible turbulence.[9,10,20,21]

Due to the non-zero nature of the first invariant (P) of the velocity gradient tensor, the flow topology in the compressible turbulence is more complex and less understood compared with the situation of the incompressible turbulence.[22–26] Suman and Girimaji[22] studied the effect of compressibility on local flow topology in decaying compressible isotropic turbulence. They found that the local flow topologies in the strong compression and expansion regions are different from those in the incompressible turbulence. Furthermore, Wang et al.[23] investigated the effect of the local compressibility on the statistical properties of the velocity gradient tensor in the highly compressible isotropic turbulence. The Helmholtz decomposition was applied to analyze the statistical properties associated with the solenoidal and dilatational component of the velocity field. Danish, Suman, and Girimaji[27] investigated the effect of the local flow topology on passive scalar mixing in the decaying compressible isotropic turbulence. It was found that the non-focal topologies induced more intense mixing than the focal topologies. Furthermore, Wang et al.[24] studied the effect of the flow topology on the subgrid-scale (SGS) kinetic energy flux in the compressible isotropic turbulence. It was shown that plenty of investigations were focused on the compressible isotropic turbulence, while the properties of the velocity gradient structures and local flow topology in the compressible wall-bounded turbulent flows were less investigated.

Wang and Lu[28] investigated the flow topology in the compressible turbulent boundary layer with the free-stream Mach number 2. It was shown that the local compressed regions tended to be more stable, and the local expanding regions were apt to be more dissipative. Moreover, the features of the average dissipation, enstrophy, dissipation production, and enstrophy production of various topologies were also investigated in the local compression and expansion regions. However, they mainly focused on the contributions of various flow topologies to the average dissipation, enstrophy, dissipation production, and enstrophy production along wall-normal direction. The alignments of vorticity with the eigenvectors of the strain rate tensor are less investigated, and the ratio of the principal strains and the contributions of various flow topologies to the eigenvalues and eigenvectors of velocity gradient tensor were never studied, which are extremely significant in figuring out the properties of small-scale motions in compressible wall-bounded flows. Chu and Lu[29]

investigated the topological evolution in the compressible turbulent boundary layer with the free-stream Mach number 2. Bechlars and Sandberg[30] studied the variation of enstrophy production and strain rotation relation in the compressible turbulent boundary layer with the free-stream Mach number 0.5. The effect of various flow topologies on the ratio of principal strains and the alignments of vorticity with the eigenvectors of strain rate tensor were investigated. However, the Mach number was too low, and the flow was similar to the incompressible turbulence. Therefore, only the flow topologies with the incompressible nature were analyzed, and the effect of compressibility on small-scale motions was not obvious in their studies. Bechlars and Sandberg[31] further studied the compressible–evolution equations for three invariants of the velocity gradient tensor. According to above introduction, the systematic investigation of the effect of local compressibility and local flow topology on the enstrophy production and velocity gradient structures are significantly necessary to understand the properties of small-scale motions in the hypersonic wall-bounded turbulence.

Recently, Xu et al.[26] investigated the contributions of various flow topologies to the subgrid-scale flux of kinetic energy in hypersonic turbulent boundary layer. They found that the direct transfer of fluctuating kinetic energy from large scales to small scales is mainly characterized by the flow topologies unstable/saddle/saddle (UN/S/S), stable focus/stretching (SFS), and stable focus/compressing (SFC) in the compression region, while the reverse transfer of fluctuating kinetic energy is primarily characterized by the flow topologies unstable focus/compressing (UFC), stable node/saddle/saddle (SN/S/S), and unstable focus/stretching (UFS) in the expansion region. However, this study was concentrated on the velocity gradient structures of the kinetic energy transfer in the inertial range; the flow structures of the velocity gradient structures of the small-scale motions in the dissipation range of the hypersonic turbulent boundary layer were less studied.

In this study, we investigate the effects of wall temperature and local compressibility on the small-scale structures, the local flow topology and the enstrophy production in the hypersonic turbulent boundary layer with isothermal wall condition. The rest of the paper is organized as follows. The governing equations and numerical methodology are introduced in Sec. II. Definitions of various local flow topologies based on the invariants of the velocity gradient tensor are presented in Sec. III. Numerical results of the local flow topology and velocity gradient structures in the hypersonic turbulent boundary layer are provided in Sec. IV. Finally, summary and conclusion are made in Sec. V.

II. GOVERNING EQS. AND NUMERICAL METHODOLOGY

We carry out direct numerical simulations of the hypersonic turbulent boundary layer by solving the following dimensionless Navier–Stokes equations in conservation form[26,32–34]

$$\frac{\partial \rho}{\partial t} + \frac{\partial (\rho u_j)}{\partial x_j} = 0, \tag{1}$$

$$\frac{\partial (\rho u_i)}{\partial t} + \frac{\partial \left[\rho u_i u_j + p \delta_{ij}\right]}{\partial x_j} = \frac{1}{Re}\frac{\partial \sigma_{ij}}{\partial x_j}, \tag{2}$$

$$\frac{\partial E}{\partial t} + \frac{\partial \left[(E+p)u_j\right]}{\partial x_j} = \frac{1}{\alpha}\frac{\partial}{\partial x_j}\left(\kappa\frac{\partial T}{\partial x_j}\right) + \frac{1}{Re}\frac{\partial (\sigma_{ij}u_i)}{\partial x_j}, \tag{3}$$

$$p = \rho T / (\gamma M^2), \tag{4}$$

where ρ is the density, u_i is the velocity component, p is the pressure, and T is the temperature. The viscous stress σ_{ij} is

$$\sigma_{ij} = \mu \left(\frac{\partial u_i}{\partial x_j} + \frac{\partial u_j}{\partial x_i} \right) - \frac{2}{3} \mu \theta \delta_{ij}, \tag{5}$$

where $\theta = \frac{\partial u_k}{\partial x_k}$ is the velocity divergence. The total energy per unit volume E is

$$E = \frac{p}{\gamma - 1} + \frac{1}{2} \rho (u_j u_j). \tag{6}$$

A set of reference scales are introduced to normalize the variables in the governing equations of the hypersonic turbulent boundary layer,[26,32–34] including the reference density ρ_∞, viscosity μ_∞, thermal conductivity κ_∞, length L_∞, freestream velocity U_∞, freestream temperature T_∞, pressure $p_\infty = \rho_\infty U_\infty^2$, and energy per unit volume $\rho_\infty U_\infty^2$. Three non-dimensional governing parameters are generated: the reference Reynolds number $Re = \rho_\infty U_\infty L_\infty / \mu_\infty$, the reference Mach number $M = U_\infty / c_\infty$, and the reference Prandtl number $Pr = \mu_\infty C_p / \kappa_\infty$. $\gamma = C_p / C_v$ is the ratio of specific heat at constant pressure C_p to that at constant volume C_v, which is assumed to be equal to 1.4. The parameter α is defined as $\alpha = Pr Re (\gamma - 1) M^2$, where Pr is assumed to be equal to 0.7.

The convection terms are discretized by a 7th-order weighted essentially non-oscillatory (WENO) scheme,[35] and the viscous terms are approximated by an 8th-order central difference scheme. A third-TVD type Runge-Kutta method is applied for time advancing.[26,32–34]

In this study, $\bar{f}$ denotes the Reynolds average (spanwise and time average) of f, and the fluctuating counterpart of the Reynolds average is $f' = f - \bar{f}$.

The schematic for the spatially developing turbulent boundary layer is plotted in Fig. 1. The hypersonic boundary layer is numerically simulated by using the following boundary conditions: the inflow and outflow boundary conditions, a wall boundary condition, an upper far-field boundary condition as well as the periodic boundary condition in the spanwise direction. Specifically, a time-independent laminar compressible boundary-layer similarity solution is applied at the inflow boundary. A region of wall blowing and suction[7] is implemented at $4.5 \leq x \leq 5$ to induce the laminar-to-turbulent transition. Moreover, all the flow fields are extrapolated from the interior points to the outflow boundary points except the pressure in the subsonic region of the boundary layer. The pressure in the subsonic region is set equal to the value of the first grid point where the flow is supersonic. It is worth noting that in order to inhibit the reflection of disturbance due to the numerical treatment of the outflow boundary condition, progressively coarse grid is applied in the streamwise direction near the outflow boundary condition.[7] Furthermore, the non-slip condition is applied for the wall, and the nonreflecting boundary condition is imposed for the upper boundary.[7] The databases analyzed in this study are extracted from the fully developed region of the hypersonic boundary layer.

Two cases including a cold wall and a less cold wall case, which are donated as M8T1 and M8T2, respectively, are analyzed in this work. The fundamental parameters are listed in Table I. Here, $M_\infty = U_\infty / c_\infty$ and $Re_\infty = \rho_\infty U_\infty L_\infty / \mu_\infty$ are the freestream Mach number and Reynolds number, respectively. T_∞ is the freestream
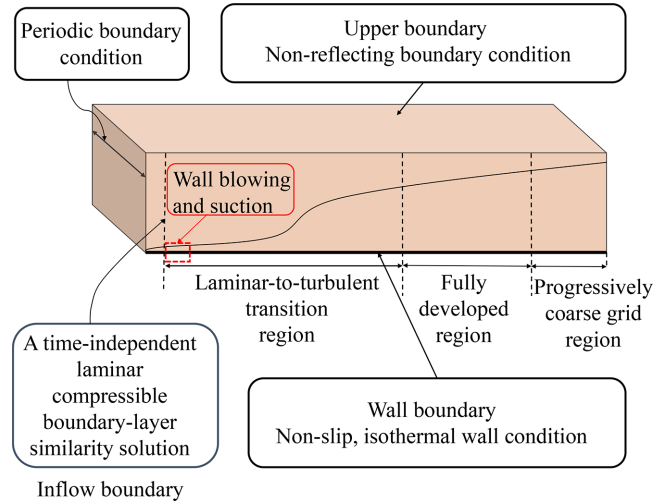

FIG. 1. The schematic of the computational domain.

temperature, which is assumed to be $T_\infty = 169.44$ K. The recovery temperature T_r is $T_r = T_\infty (1 + r ((\gamma - 1)/2) M_\infty^2)$ with recovery factor $r = 0.9$.[4] T_w is the wall temperature. The computational domains L_x, L_y, and L_z are nondimensionalized by $L_\infty = 1$ $inch$.[7] x, y, and z are the streamwise, wall-normal and spanwise directions, respectively. $\delta_\nu = \bar{\mu}_w / (\bar{\rho}_w u_\tau)$ is the viscous lengthscale. $u_\tau = \sqrt{\tau_w / \rho_w}$ is the friction velocity. $\bar{\mu}_w$ and $\bar{\rho}_w$ are the Reynolds average of the viscosity and density on the wall, respectively. $\tau_w = (\mu \frac{\partial \bar{U}}{\partial y})_{y=0}$ is the wall shear stress. $\Delta x^+ = \Delta x / \delta_\nu$, $\Delta y_w^+ = \Delta y_w / \delta_\nu$, and $\Delta z^+ = \Delta z / \delta_\nu$ are the normalized spacing of the streamwise direction, the first point off the wall, and the spanwise direction, respectively. Furthermore, y^+ is defined as $y^+ \equiv y / \delta_\nu$; y^* is defined as $y^* \equiv y / \delta_\tau^*$, where $\delta_\tau^* = \bar{\mu} / (\bar{\rho} u^*)$ is the semilocal scaling and $u^* = \sqrt{\tau_w / \bar{\rho}}$.

Data in a small streamwise window of $[x_a - 0.5\delta, x_a + 0.5\delta]$ extracted from the fully developed region of the hypersonic turbulent boundary layer is used for calculating flow statistics. Here, $x_a = 14$ and 30 for M8T1 and M8T2, $\delta = 0.13$ and 0.28 for M8T1 and M8T2, respectively. 1000 flow-field snapshots spanning a time interval of approximately $140\delta / U_\infty$ are used for analysis.

The Helmholtz decomposition is applied to decompose the velocity field ($\mathbf{u}$) into a solenoidal ($\mathbf{u}_s$) and a dilatational ($\mathbf{u}_d$) component ($\mathbf{u} = \mathbf{u}_s + \mathbf{u}_d$), which satisfies $\nabla \cdot \mathbf{u}_s = 0$ and $\nabla \times \mathbf{u}_d = 0$,

TABLE I. Summary of computational parameters for the DNS cases. The computational domains L_x, L_y, and L_z are nondimensionalized by 1 *inch*. (Pirozzoli *et al.*[7]).

Case	M_∞	Re_∞	T_w / T_∞	T_w / T_r	$L_x \times L_y \times L_z$
M8T1	8	2×10^6	1.9	0.15	$19 \times 0.7 \times 0.35$
M8T2	8	5×10^6	10.03	0.80	$41 \times 0.7 \times 0.6$

Case	$N_x \times N_y \times N_z$	Δx^+	Δy_w^+	Δz^+
M8T1	$9000 \times 200 \times 1280$	11.2	0.5	4.5
M8T2	$12\,500 \times 200 \times 640$	12.2	0.5	4.6

respectively. The two components can be obtained by solving the Poisson equations of the vector potential $\mathbf{A}$ and scalar potential φ, which are expressed as

$$\nabla^2 \mathbf{A} = -\nabla \times \mathbf{u}, \quad \nabla^2 \varphi = \nabla \cdot \mathbf{u}. \tag{7}$$

Consequently, the solenoidal and dilatational components can be procured by

$$\mathbf{u}_s = \nabla \times \mathbf{A}, \quad \mathbf{u}_d = \nabla \varphi. \tag{8}$$

Under the following wall boundary conditions given by Hirasaki and Hellums,[36]

$$\frac{\partial \varphi}{\partial y} = 0, \quad \frac{\partial A_y}{\partial y} = 0, \quad A_x = A_z = 0, \tag{9}$$

the vector potential $\mathbf{A}$ is unique.[8,36–39] A mirror symmetry is implemented on the data in a pretty large streamwise window of $[x_a - 4\delta, x_a + 4\delta]$ to generate an artificial periodic condition in the streamwise direction. It is worth noting that the artificial periodic condition has little effect on the flow statistics of the data in a small streamwise window of $[x_a - 0.5\delta, x_a + 0.5\delta]$. If the streamwise window is further increased to $[x_a - 8\delta, x_a + 8\delta]$, the flow statistics of the data in $[x_a - 0.5\delta, x_a + 0.5\delta]$ is unchanged. Then, the Poisson equations (7) are discretized spectrally in the streamwise (x) and spanwise (z) directions, and by a 6th-order central difference scheme in the wall-normal (y) direction. It is noted that the Helmholtz decomposition has been validated in Xu et al.[32,33] previously.

The velocity field can be decomposed into $\mathbf{u} = \bar{\mathbf{U}} + \mathbf{u}'$, where $\bar{\mathbf{U}}$ is the Reynolds average of velocity field and $\mathbf{u}'$ is the fluctuating counterpart. Furthermore, the fluctuating counterpart can be divided into a solenoidal ($\mathbf{u}_s'$) and a dilatational ($\mathbf{u}_d'$) component based on the Helmholtz decomposition.

Several relevant Reynolds numbers are significant in the compressible turbulent boundary layer. The friction Reynolds number $Re_\tau = \bar{\rho}_w u_\tau \delta / \bar{\mu}_w$ is defined as the ratio of the boundary layer thickness to the viscous lengthscale. The Reynolds number based on the momentum thickness θ_{th} and the wall viscosity, $Re_{\delta_2} = \rho_\infty u_\infty \theta_{th} / \bar{\mu}_w$, is defined as the ratio of the highest momentum to the wall shear stress. Here, the momentum thickness θ_{th} is defined as

$$\theta_{th} = \int_0^\delta \frac{\bar{\rho} \bar{u}}{\rho_\infty U_\infty} \left(1 - \frac{\bar{u}}{U_\infty} \right) dy. \tag{10}$$

$Re_{\theta_{th}} = \rho_\infty u_\infty \theta_{th} / \mu_\infty$ is the Reynolds number based on the momentum thickness θ_{th}. The global flow properties are listed in Table II. Furthermore, the grid convergence studies of the database are shown in Appendix, and the adequacy of the computational domain size in the spanwise direction has been confirmed in Xu et al.[26,32,33]

The normalized fluctuating velocity divergence is defined as $\theta'^+ = \theta'/(u_\tau/\delta_\nu)$, where $\theta' = \nabla \cdot \mathbf{u}'$. The probability density

TABLE II. Global flow properties.

Case	Re_∞	Re_τ	$Re_{\theta_{th}}$	Re_{δ_2}
M8T1	2×10^6	2444	1.02×10^4	6018
M8T2	5×10^6	1386	3.22×10^4	6563

functions (PDFs) of the normalized fluctuating velocity divergence θ'^+ along the wall-normal direction are plotted in Fig. 2. It is shown that the fluctuating velocity divergence is strong near the wall and much weak far from the wall, indicating that the compressibility effect is strong in the near wall region.[32,33] Moreover, the PDF of θ'^+ in M8T2 is nearly symmetric near the wall, while PDF of θ'^+ in M8T1 exhibits the strong negative skewness, indicating that the colder wall temperature significantly enhances the compression motions near the wall.[32,33] In the far wall region, PDFs of θ'^+ in M8T1 and M8T2 are similar, indicating that the effect of wall temperature on the compressibility effect is concentrated on the near wall region.[32,33]

III. LOCAL FLOW TOPOLOGY OF COMPRESSIBLE TURBULENCE

Based on the topological classification by Chong et al.,[15] the local flow pattern at a point in the compressible turbulence can be inferred by three invariants of the velocity gradient tensor $A_{ij} = \partial u_j / \partial x_i$. The eigenvalues ξ_i of the velocity gradient tensor A_{ij} satisfy the characteristic equation

$$\xi_i^3 + P \xi_i^2 + Q \xi_i + R = 0, \tag{11}$$

where P, Q, and R are the first, second, and third invariants of A_{ij}, which are written as

$$P = -(\xi_1 + \xi_2 + \xi_3) = -tr(A_{ij}) = -S_{ii} = -\theta, \tag{12a}$$

$$Q = \xi_1 \xi_2 + \xi_2 \xi_3 + \xi_3 \xi_1 = \frac{1}{2} \left([tr(A_{ij})]^2 - tr(A_{ij}^2) \right)$$
$$= \frac{1}{2} \left(P^2 - S_{ij} S_{ji} - W_{ij} W_{ji} \right), \tag{12b}$$

$$R = -\xi_1 \xi_2 \xi_3 = -det(A_{ij})$$
$$= \frac{1}{3} \left(-P^3 + 3PQ - S_{ij} S_{jk} S_{ki} - 3 W_{ij} W_{jk} S_{ki} \right), \tag{12c}$$

where $S_{ij} = (A_{ij} + A_{ji})/2$ is the strain rate tensor and $W_{ij} = (A_{ij} - A_{ji})/2$ is the rotation rate tensor. It is worth noting that they are the symmetric part and skew-symmetric part of the velocity gradient tensor A_{ij}, respectively. $\theta = \nabla \cdot \mathbf{u}$ is the velocity divergence.

The invariants of S_{ij} and W_{ij} are shown as

$$P_S = P = -S_{ii}, \quad Q_S = \frac{1}{2} \left(P_S^2 - S_{ij} S_{ji} \right),$$
$$R_S = \frac{1}{3} \left(-P_S^3 + 3 P_S Q_S - S_{ij} S_{jk} S_{ki} \right), \tag{13a}$$

$$P_W = 0, \quad Q_W = -\frac{1}{2} W_{ij} W_{ji}, \quad R_W = 0. \tag{13b}$$

The invariants defined above satisfy

$$Q = Q_S + Q_W, \quad R = R_S - W_{ij} W_{jk} S_{ki} = R_S - \frac{1}{4} \omega_i S_{ij} \omega_j, \tag{14}$$

where $\omega_i S_{ij} \omega_j$ is the enstrophy production.

The discriminant Δ of the velocity gradient tensor A_{ij} is written as

$$\Delta = 27 R^2 + \left(4 P^3 - 18 PQ \right) R + \left(4 Q^3 - P^2 Q^2 \right). \tag{15}$$

It is noted that if $\Delta < 0$, A_{ij} has three real eigenvalues: $\xi_1 \leq \xi_2 \leq \xi_3$. On the other hand, if $\Delta > 0$, A_{ij} has one real eigenvalue and two
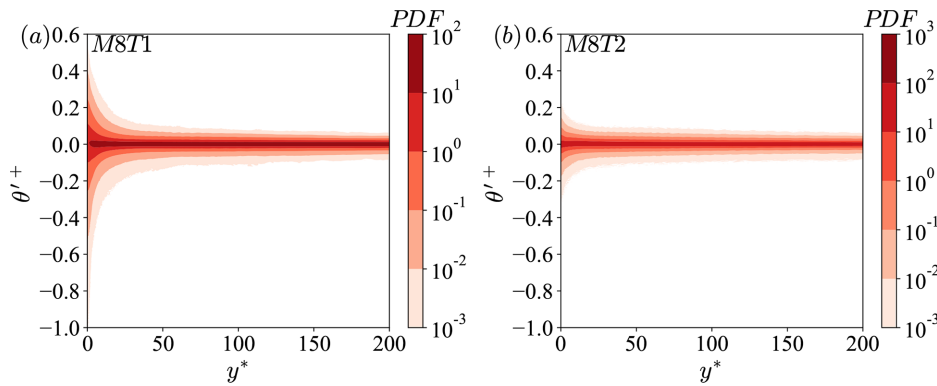
FIG. 2. PDF of the normalized fluctuating velocity divergence θ'^{+} along the wall-normal direction in (a) M8T1 and (b) M8T2.

complex conjugate pairs: $\xi_{1,2} = \xi_r \pm i\xi_i$, and ξ_3 is real, where ξ_r and ξ_i are real numbers.[15]

The surface $\Delta = 0$ can be split into two surfaces $r^{(1a)}$ and $r^{(1b)}$, which are defined as

$$P(9Q - 2P^2) - 2(-3Q + P^2)^{3/2} - 27R = 0, \qquad (16a)$$

$$P(9Q - 2P^2) + 2(-3Q + P^2)^{3/2} - 27R = 0. \qquad (16b)$$

They osculate each other to form a cusp. Moreover, in the region $\Delta > 0$, another surface $r^{(2)}$ contains the points representing the purely imaginary eigenvalues, which can be shown by

$$PQ - R = 0. \qquad (17)$$

Therefore, the P–Q–R space can be divided into different spatial regions by the surfaces $r^{(1a)}$, $r^{(1b)}$, $r^{(2)}$, and $R = 0$, and each region can be related to a specific topology.[15]

The flow topology can be studied in the Q–R plane for a selected value of P or θ.[22,28] Therefore, the surfaces $r^{(1a)}$, $r^{(1b)}$, $r^{(2)}$, and $R = 0$ divide the Q–R plane into various regions associated with different topologies. The topological classifications of three representative Q–R planes ($P = 0$, $P > 0$, and $P < 0$) are plotted in Fig. 3. The descriptions of acronyms for various flow topologies are listed in Table III.[22,28]

It is shown in Fig. 3(a) that on the plane $P = 0$, the curves $r^{(1a)}$ and $r^{(1b)}$ are symmetric in regard to the curve $R = 0$, and the curve $r^{(2)}$ is consistent with the $R = 0$ curve. Therefore, there are four different topologies: UFC, UN/S/S, SN/S/S, and SFS, which are represented

by $S^{(1)}$, $S^{(2)}$, $S^{(3)}$, and $S^{(4)}$, respectively. It is worth noting that the "stable" indicates that the solution trajectories or the local streamlines of local velocity gradient tensor are directed toward the critical point, while the "unstable" suggests that the solution trajectories or the local streamlines are pointed away from the critical point.[22] Therefore, the stable topologies indicate that the fluid element tends to be compressive, while the unstable topologies imply that the fluid element tends to be expansive. It should be noted that for positive Δ, the fluid element represents a structure with rotational characteristic and an out-of-plane strain. On the other hand, if $\Delta < 0$, the fluid element appears to be non-swirling and straining. Moreover, for positive third invariant R, the fluid element exhibits the structure with two stretching directions and one contracting direction, while if $R < 0$, the fluid element represents the structure with two contracting directions and one stretching direction.[30] The signs of the three eigenvalues of velocity gradient tensor A_{ij} in above four topologies are listed as follows: $\xi_r > 0$ and $\xi_3 < 0$ for UFC; $\xi_r < 0$ and $\xi_3 > 0$ for SFS; $\xi_1 < 0$, $\xi_2 > 0$, and $\xi_3 > 0$ for UN/S/S; $\xi_1 < 0$, $\xi_2 > 0$, and $\xi_3 > 0$ for UN/S/S; $\xi_1 < 0$, $\xi_2 < 0$, and $\xi_3 > 0$ for SN/S/S. Therefore, the UFC topology represents an expansive vortical structure with an out-of-plane contracting strain. The SFS topology implies a compressive vortical structure with an out-of-plane stretching strain. The UN/S/S topology exhibits the non-swirling, straining structure with two stretching directions and one contracting direction. The SN/S/S topology reveals the non-swirling, straining structure with two contracting directions and one stretching direction.
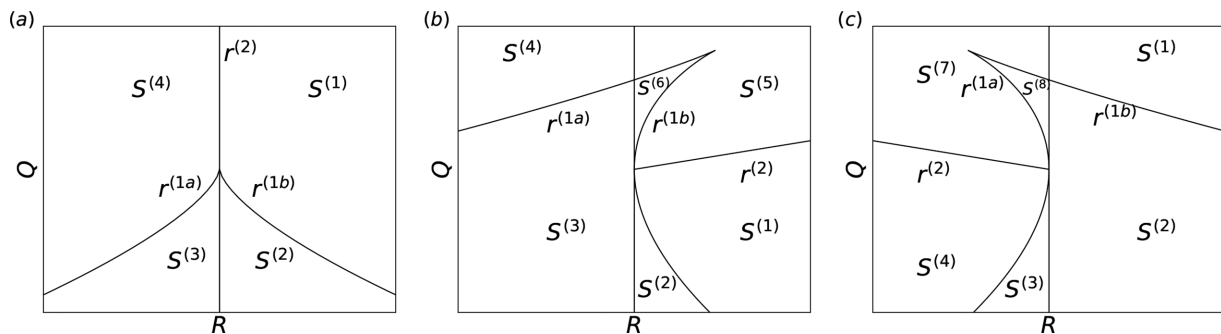

FIG. 3. The topological classifications of three representative Q–R planes: (a) $P = 0$, (b) $P > 0$, and (c) $P < 0$. The description of acronyms for various flow topologies is provided in Table III.

TABLE III. Description of acronyms for various flow topologies.

Sector	Acronym	Description
$S^{(1)}$	UFC	Unstable focus/compressing
$S^{(2)}$	UN/S/S	Unstable node/saddle/saddle
$S^{(3)}$	SN/S/S	Stable node/saddle/saddle
$S^{(4)}$	SFS	Stable focus/stretching
$S^{(5)}$	SFC	Stable focus/compressing
$S^{(6)}$	SN/SN/SN	Stable node/stable node/stable node
$S^{(7)}$	UFS	Unstable focus/stretching
$S^{(8)}$	UN/UN/UN	Unstable node/unstable node/unstable node

It is seen in Fig. 3(b) that on the plane $P > 0$, the curves $r^{(1a)}$ and $r^{(1b)}$ are not symmetric, and the curve $r^{(2)}$ intersects with the $r^{(1b)}$ curve at $Q = 0$ and $R = 0$. There are six different topologies in the Q–R plane: UFC, UN/S/S, SN/S/S, SFS, SFC, and SN/SN/SN, which are denoted by $S^{(1)}$, $S^{(2)}$, $S^{(3)}$, $S^{(4)}$, $S^{(5)}$, and $S^{(6)}$, respectively. It is noted that $\xi_r < 0$ and $\xi_3 < 0$ for SFC, and $\xi_1 < 0$, $\xi_2 < 0$, and $\xi_3 < 0$ for SN/SN/SN. Accordingly, the SFC topology is associated with a compressive vortical structure with an out-of-plane contracting strain. The SN/SN/SN topology represents a sink flow with all streamlines converging radially to the center of the fluid element, which results in a decrease in volume. This topology can be considered as a rotation-free, isotropic compression of a fluid element.[22]

Furthermore, on the plane $P < 0$ shown in Fig. 3(c), the curve $r^{(2)}$ intersects with the $r^{(1a)}$ curve at $Q = 0$ and $R = 0$. There are six different topologies in the Q–R plane: UFC, UN/S/S, SN/S/S, SFS, UFS, and UN/UN/UN, which are denoted by $S^{(1)}$, $S^{(2)}$, $S^{(3)}$, $S^{(4)}$, $S^{(7)}$, and $S^{(8)}$, respectively. It is worth noting that $\xi_r > 0$ and $\xi_3 > 0$ for UFS, while $\xi_1 > 0$, $\xi_2 > 0$, and $\xi_3 > 0$ for UN/UN/UN. Thus, the UFS topology implies an expansive vortical structure with an out-of-plane stretching strain. The UN/UN/UN indicates a source flow with all streamlines diverging radially from the center of the fluid element, which leads to an increase in volume. This topology can be viewed as a rotation-free, isotropic expansion of a fluid element.[22]

Furthermore, the fluctuating velocity gradient tensor is defined by $A'_{ij} = \partial u'_j / \partial x_i$. By definition, the three eigenvalues ξ'_i satisfy the following characteristic equation:

$$\xi'^3_i + P' \xi'^2_i + Q' \xi'_i + R' = 0, \tag{18}$$

where P', Q', and R' are the first, second, and third invariants of A'_{ij}, which are defined by

$$P' = -\theta', \tag{19a}$$

$$Q' = \frac{1}{2} \left(P'^2 - S'_{ij} S'_{ji} - W'_{ij} W'_{ji} \right), \tag{19b}$$

$$R' = \frac{1}{3} \left(-P'^3 + 3P'Q' - S'_{ij} S'_{jk} S'_{ki} - 3W'_{ij} W'_{jk} S'_{ki} \right), \tag{19c}$$

where $S'_{ij} = (A'_{ij} + A'_{ji})/2$ is the fluctuating strain rate tensor and $W'_{ij} = (A'_{ij} - A'_{ji})/2$ is the fluctuating rotation rate tensor. Accordingly, the relevant eight flow topologies $S'^{(k)}$ of the fluctuating velocity gradient tensor A'_{ij} can also be obtained from the relevant P'–Q'–R' space.

IV. NUMERICAL RESULTS OF LOCAL FLOW TOPOLOGY

A. Statistical properties of the invariants of the velocity gradient tensor

The statistical properties of the velocity gradient tensor can be investigated in terms of the joint PDFs of the second and third invariants for selected values of P. Three typical values of $P^+ = P/(u_\tau / \delta_\nu)$, i.e., $P^+ = 0$, 0.02, and -0.02, are selected to analyze the joint PDFs in Q–R plane. The typical values $P^+ = 0.02$ and -0.02 represent the performance in the strong compression and expansion regions. The second (Q) and third (R) invariants of the velocity gradient tensor can be normalized by $\langle Q_W \rangle$ and $\langle Q_W \rangle^{3/2}$, respectively.

Figure 4 depicts the joint PDFs of Q and R in the buffer layer and logarithmic layer in M8T1 and M8T2 for three typical values of $P^+ = 0$, 0.02, and -0.02. It is found that in the buffer layer where the mean shear is relatively high, the contours of the joint PDFs are much thinner compared with those in the logarithmic layer, which is consistent with the observations in the supersonic turbulent boundary layer.[28] Furthermore, the contours of the joint PDFs for $P^+ = 0$ exhibit self-similar teardrop shapes around the origin, which is similar to those observed in the incompressible turbulent flows,[14,16–18,40] compressible isotropic turbulence,[22,41] and supersonic turbulent boundary layer.[28]

The contours of the joint PDFs of Q and R in the compression region $P^+ = 0.02$ become more symmetric, and the fractions of the contours occupying the first and third quadrants become larger compared with those in $P^+ = 0$. In contrast, the contours of the joint PDFs in the expansion region $P^+ = -0.02$ have a tendency to occupy the second and fourth quadrants and demonstrate more skewed shapes compared with those in $P^+ = 0$. It is also found that the joint PDFs of Q and R for $P^+ > 0$ and $P^+ < 0$ in M8T1 deviate from that for $P^+ = 0$ more significantly than those in M8T2. Furthermore, the joint PDFs of Q and R for $P^+ > 0$ and $P^+ < 0$ in M8T2 are more scattered than those in M8T1, mainly due to weak compressibility and lack of points in the strong compression and expansion regions in M8T2.

B. Flow topology and its contribution to the enstrophy production

The statistical properties in P–Q–R space can be described conveniently by the volume fractions $V_f^{(k)}$ of various flow topologies $S^{(k)}$ in the hypersonic turbulent boundary layer. Conditional volume fractions $\langle V_r^{(k)} | P^+ > 0 \rangle$ and $\langle V_r^{(k)} | P^+ < 0 \rangle$ for the compression and expansion regions, respectively, are also investigated to clarify the compressibility effect on the flow topologies. Here, $V_f^{(k)} = V_{S_k} / V_{all}$, where V_{S_k} is the volume of flow topology $S^{(k)}$ and V_{all} is the total volume. $\langle V_r^{(k)} | P^+ > 0 \rangle = \langle V_{S_k} | P^+ > 0 \rangle / V_{all}$, where $\langle V_{S_k} | P^+ > 0 \rangle$ is the volume of flow topology $S^{(k)}$ in the compression region $P^+ > 0$.

Volume fractions $V_f^{(k)}$ and conditional volume fractions of various flow topologies $S^{(k)}$ along the wall-normal direction are plotted in Fig. 5. It is found that the volume fractions and conditional volume fractions vary sharply along y^* near the wall where the mean shear is high and change slowly in the far-wall region where the mean shear is relatively low.[28] Furthermore, the volume fractions and conditional volume fractions in M8T1 and M8T2 are similar far from the wall, while are distinctive near the wall due to different wall temperatures, indicating that the wall temperature has a significant influence on the
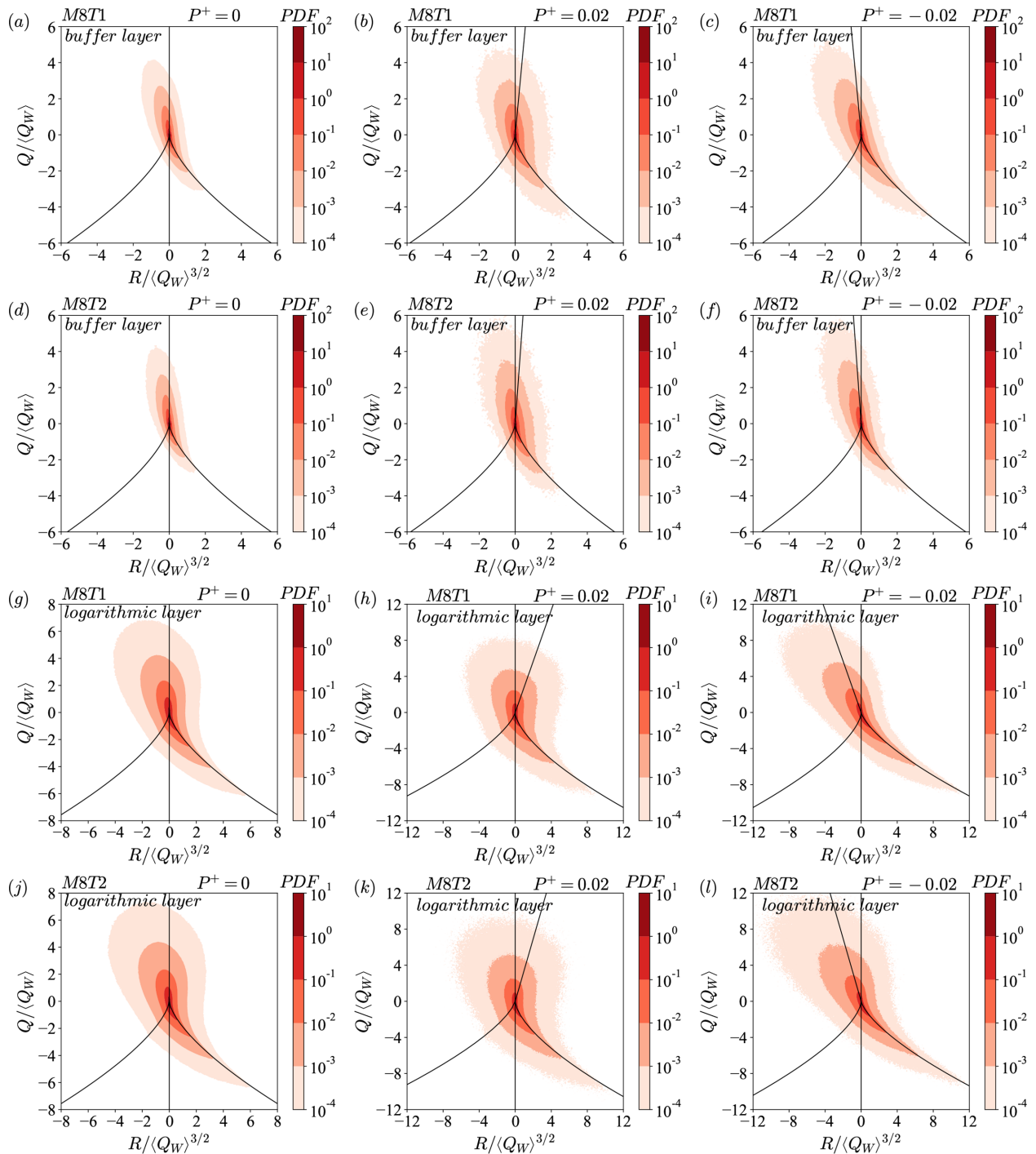
FIG. 4. Joint PDFs of Q and R in the buffer layer (a)–(f) and logarithmic layer (g)–(l).

local flow topology in the near-wall region and has the negligible effect in the far wall region.

The sum of the volume fractions of unstable topologies ($S^{(1)}$, $S^{(2)}$, $S^{(7)}$, and $S^{(8)}$) is slightly larger than that of stable topologies ($S^{(3)}$, $S^{(4)}$, $S^{(5)}$, and $S^{(6)}$) across the boundary layer, indicating that the flow is favorable to be expansive and unstable.[28] Moreover, it is found that the cold wall significantly enhances the sum of the volume fractions of unstable topologies near the wall, which can be explained as
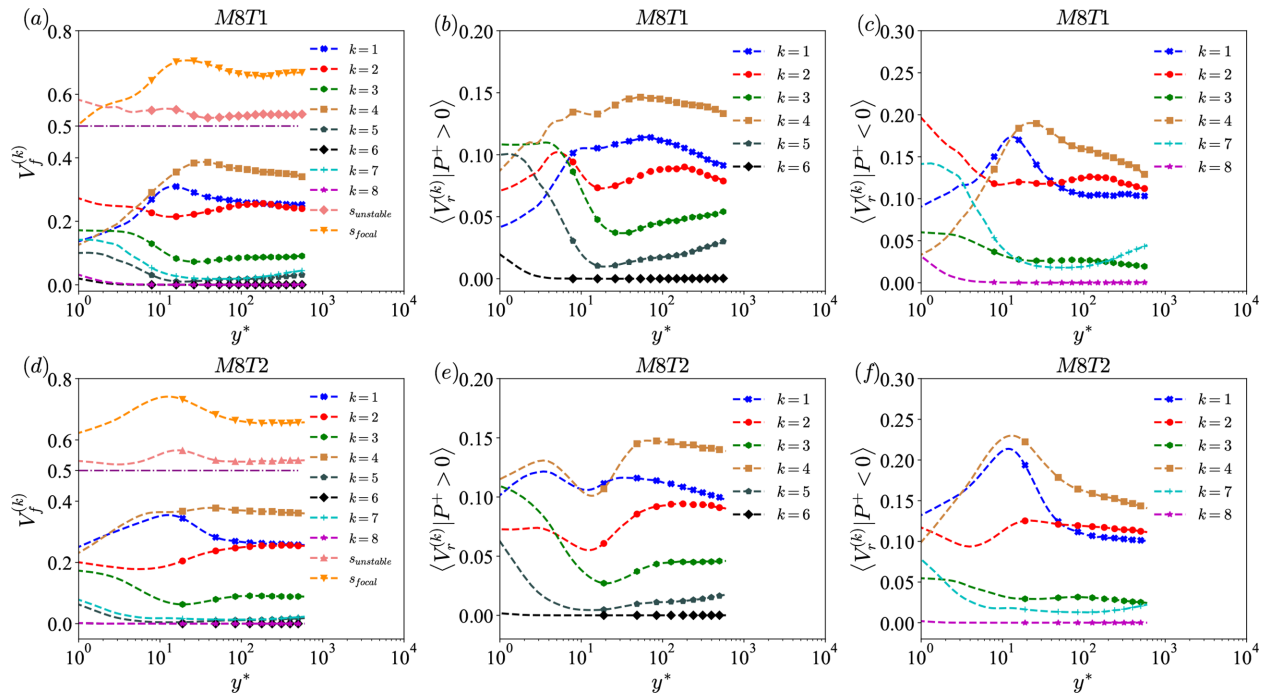
FIG. 5. (a) and (d): The volume fractions of various flow topologies $S^{(k)}$ along the wall-normal direction in (a) M8T1 and (d) M8T2. (b) and (e): The volume fractions of various flow topologies $S^{(k)}$ conditioned on $P^+ > 0$ along the wall-normal direction in (b) M8T1 and (e) M8T2. (c) and (f): The volume fractions of various flow topologies $S^{(k)}$ conditioned on $P^+ > 0$ along the wall-normal direction in (c) M8T1 and (f) M8T2. It is noted that the label "$s_{unstable}$" represents the sum of the volume fractions of unstable topologies ($S^{(1)}$, $S^{(2)}$, $S^{(7)}$, and $S^{(8)}$), and the label "s_{focal}" represents the sum of the volume fractions of focal topologies ($S^{(1)}$, $S^{(4)}$, $S^{(5)}$, and $S^{(7)}$) in (a) and (d).

follows: It is known that the cold wall significantly enhances the compression motions near the wall[32,33] and accordingly results in a rapid decrease in the volume of fluid element and an increase in the sum of the volume fractions of unstable topologies. The focal topologies ($S^{(1)}$, $S^{(4)}$, $S^{(5)}$, and $S^{(7)}$) are dominant across the boundary layer, indicating that the vortical structures play the major role across the hypersonic turbulent boundary layer. Furthermore, the cold wall drastically decreases the sum of the volume fractions of the focal topologies ($S^{(1)}$, $S^{(4)}$, $S^{(5)}$, and $S^{(7)}$) near the wall, which mainly due to the reason that the cold wall increases the compression motions near the wall, and the compression motions exhibit sheet-like structures. The enhanced sheet-like structures are mainly governed by the non-swirling, straining structures, which consequently increase the volume fractions of non-focal topologies ($S^{(2)}$, $S^{(3)}$, $S^{(6)}$, and $S^{(8)}$).

It is shown in Figs. 5(a) and 5(d) that in the far-wall region, $S^{(4)}$ is the most dominant flow pattern, and $S^{(1)}$ and $S^{(2)}$ are also the predominant flow patterns. The topologies $S^{(5)}$, $S^{(6)}$, $S^{(7)}$, and $S^{(8)}$ can be observed only for compressible flows. Accordingly, the volume fractions of $S^{(5)}$ and $S^{(7)}$ are negligibly small, and fractions of $S^{(6)}$ and $S^{(8)}$ are almost zero far from the wall due to weak compressibility. However, in the near-wall region, the flow patterns are totally different in M8T1 and M8T2. It is shown that in M8T2, the topologies $S^{(1)}$ and $S^{(4)}$ are the most dominant flow patterns near the wall, while the volume fractions of $S^{(6)}$ and $S^{(8)}$ are almost zero due to weak compressibility, which is consistent with the observations in the supersonic turbulent boundary layer.[28] However, in M8T1, the percentages of $S^{(1)}$ and $S^{(4)}$ decrease sharply while that of $S^{(2)}$ increases with colder wall

temperature, leading to the dominance of flow topology $S^{(2)}$ in the near-wall region. Due to the stronger near-wall compressibility with colder wall temperature, all four compressible-relevant topologies $S^{(5)}$, $S^{(6)}$, $S^{(7)}$, and $S^{(8)}$ increase drastically in the near-wall region in M8T1.

It is found in Figs. 5(b), 5(c), 5(e), and 5(f) that the volume fractions of $S^{(1)}$, $S^{(2)}$, $S^{(3)}$, and $S^{(4)}$ for $P^+ > 0$ and $P^+ < 0$ are similar far from the wall, where $S^{(1)}$, $S^{(2)}$, and $S^{(4)}$ topologies are dominant, indicating that the volume fractions of flow topologies have weak correlation with local compressibility far from the wall. Significant differences of conditional volume fractions between $P^+ > 0$ and $P^+ < 0$ only appear in the near-wall region. Stable topologies $S^{(3)}$, $S^{(4)}$, and $S^{(5)}$ are predominant in the compression region ($P^+ > 0$), while unstable topologies $S^{(1)}$, $S^{(2)}$, and $S^{(7)}$ are favorable in the expansion region ($P^+ < 0$). Typically, due to strong compressibility near the wall in M8T1, compressible-relevant topologies $S^{(5)}$ and $S^{(7)}$ occupy a large proportion in $P^+ > 0$ and $P^+ < 0$, respectively, which is different from the observation in Wang and Lu.[28]

Relative contributions of various topologies to the enstrophy production are also investigated. We define the relative contributions $C_\alpha^{(k)}$ of various flow topologies $S^{(k)}$ to the average of variable $\langle \alpha \rangle$ as follows: $C_\alpha^{(k)} = \alpha / \langle \alpha \rangle$ if the point is located in the topology $S^{(k)}$; otherwise, $C_\alpha^{(k)} = 0$. Here, α represents the enstrophy production $\omega_i S_{ij} \omega_j$.

The average of relative contributions $C_{\omega_i S_{ij} \omega_j}^{(k)}$ of various flow topologies $S^{(k)}$ to $\langle \omega_i S_{ij} \omega_j \rangle$ as well as the average of relative contributions $C_{\omega_i S_{ij} \omega_j}^{(k)}$ conditioned on $P^+ > 0$ and $P^+ < 0$ along the

wall-normal direction are plotted in Fig. 6. It is found that the enstrophy production $\omega_i S_{ij} \omega_j$ is primarily contributed by the focal topologies ($S^{(1)}$, $S^{(4)}$, $S^{(5)}$, and $S^{(7)}$) in most of regions. Moreover, the positive enstrophy production is mainly contributed by $S^{(2)}$ and $S^{(4)}$, while the negative enstrophy production (enstrophy destruction) is primarily caused by $S^{(5)}$. In M8T1, $S^{(7)}$ also plays a major role in the contribution to the positive $\omega_i S_{ij} \omega_j$ in the near-wall region, due to strong compressibility with colder wall temperature. Accordingly, it is concluded that the enstrophy production near the wall is mainly generated by the non-swirling, straining structure with two stretching directions and the compressive vortical structure with an out-of-plane stretching strain, which indicates that the enstrophy production is highly associated with the stretching structures. In the near-wall region, the dominant sheet-like structures exhibit the strong strain, giving rise to the major contribution of topology $S^{(2)}$ to enstrophy production. As the wall distance increases, tube-like structures become dominant instead of sheet-like structures, resulting in the dominance of topology $S^{(4)}$ in producing enstrophy. Moreover, it is noted that the enstrophy destruction mainly concentrates in the near-wall region and is strongly correlated with the compressive vortical structure with an out-of-plane contracting strain. Furthermore, the flow topologies $S^{(4)}$ and $S^{(5)}$ mainly contribute to $\omega_i S_{ij} \omega_j$ in compression region ($P^+ > 0$), while $S^{(2)}$ and $S^{(7)}$ have the major contributions to $\omega_i S_{ij} \omega_j$ in expansion region ($P^+ < 0$) near the wall.

The contour of the normalized enstrophy production $\omega_i S_{ij} \omega_j^+$ at $y^* = 8$ is shown in Figs. 7(a) and 7(b). It is seen that the enstrophy destruction (negative $\omega_i S_{ij} \omega_j^+$) region exhibits the sheet-like structures, while the enstrophy production (positive $\omega_i S_{ij} \omega_j^+$) region is much fatter than the enstrophy destruction region. The streamwise-spanwise averages of the normalized enstrophy production $\omega_i S_{ij} \omega_j^+$ conditioned on the normalized fluctuating velocity divergence θ'^+ along wall-normal direction y^* are shown in Figs. 7(c) and 7(d). It is shown that in the near wall region, the conditional average $\langle \omega_i S_{ij} \omega_j^+ | \theta'^+ \rangle$ is negative in strong compression region, implying that the interaction between the vorticity and the strain-rate tensor causes the destruction of the enstrophy in strong compression region; whereas the conditional average $\langle \omega_i S_{ij} \omega_j^+ | \theta'^+ \rangle$ is positive in strong expansion region, suggesting that strong expansion motions enhance the production of the enstrophy by the interaction between the vorticity and the strain-rate tensor. However, the normalized enstrophy production $\omega_i S_{ij} \omega_j^+$ has weak correlation with the local fluctuating velocity divergence θ'^+ far from the wall, mainly due to weak compressibility in the far wall region.[4,32,33] The above statistical properties are consistent with the flow structures shown in Figs. 7(a) and 7(b). The enstrophy destruction region exhibits sheet-like structures, which is in accordance with the fact that the enstrophy destruction prefers to be situated in the compression region. However, the enstrophy
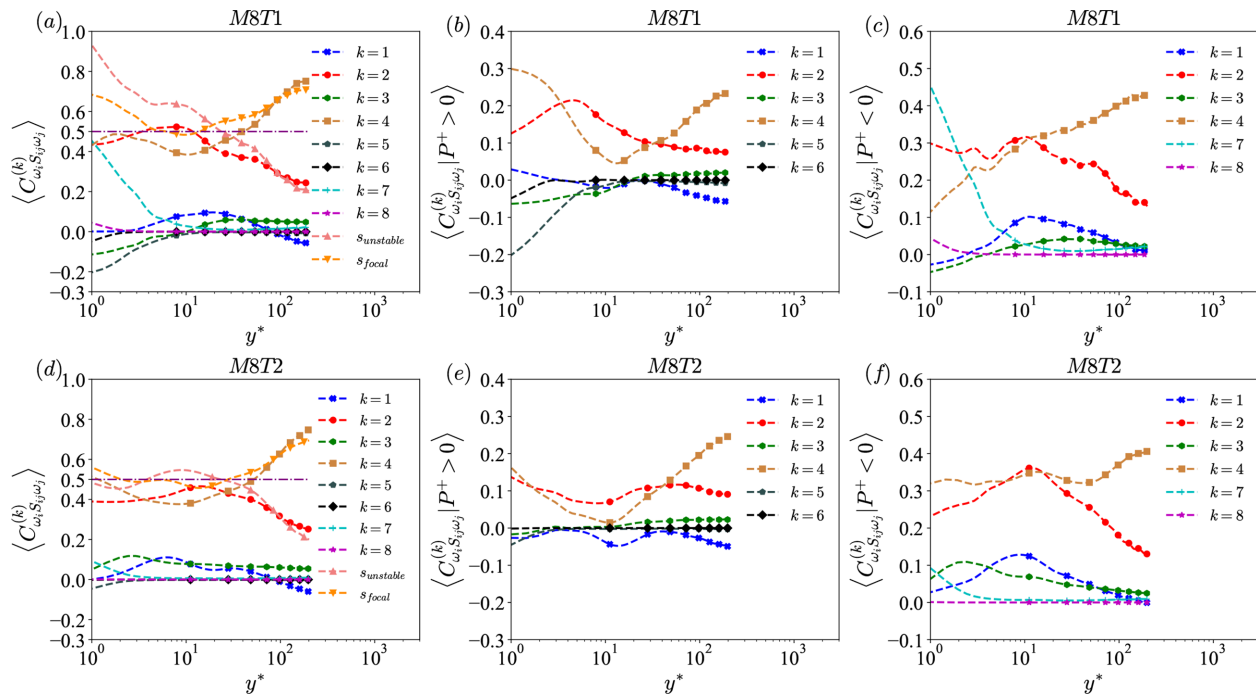

FIG. 6. (a) and (d): The average of relative contributions $C_{\omega_i S_{ij} \omega_j}^{(k)}$ of various flow topologies $S^{(k)}$ to $\langle \omega_i S_{ij} \omega_j \rangle$ along the wall-normal direction in (a) M8T1 and (d) M8T2. (b) and (e): The average of relative contributions $C_{\omega_i S_{ij} \omega_j}^{(k)}$ of various flow topologies $S^{(k)}$ to $\langle \omega_i S_{ij} \omega_j \rangle$ conditioned on $P^+ > 0$ along the wall-normal direction in (b) M8T1 and (e) M8T2. (c) and (f): The average of relative contributions $C_{\omega_i S_{ij} \omega_j}^{(k)}$ of various flow topologies $S^{(k)}$ to $\langle \omega_i S_{ij} \omega_j \rangle$ conditioned on $P^+ > 0$ along the wall-normal direction in (c) M8T1 and (f) M8T2. It is noted that the label "$s_{unstable}$" represents the sum of the relative contributions of unstable topologies ($S^{(1)}$, $S^{(2)}$, $S^{(7)}$, and $S^{(8)}$), and the label "s_{focal}" represents the sum of the relative contributions of focal topologies ($S^{(1)}$, $S^{(4)}$, $S^{(5)}$, and $S^{(7)}$) in (a) and (d).
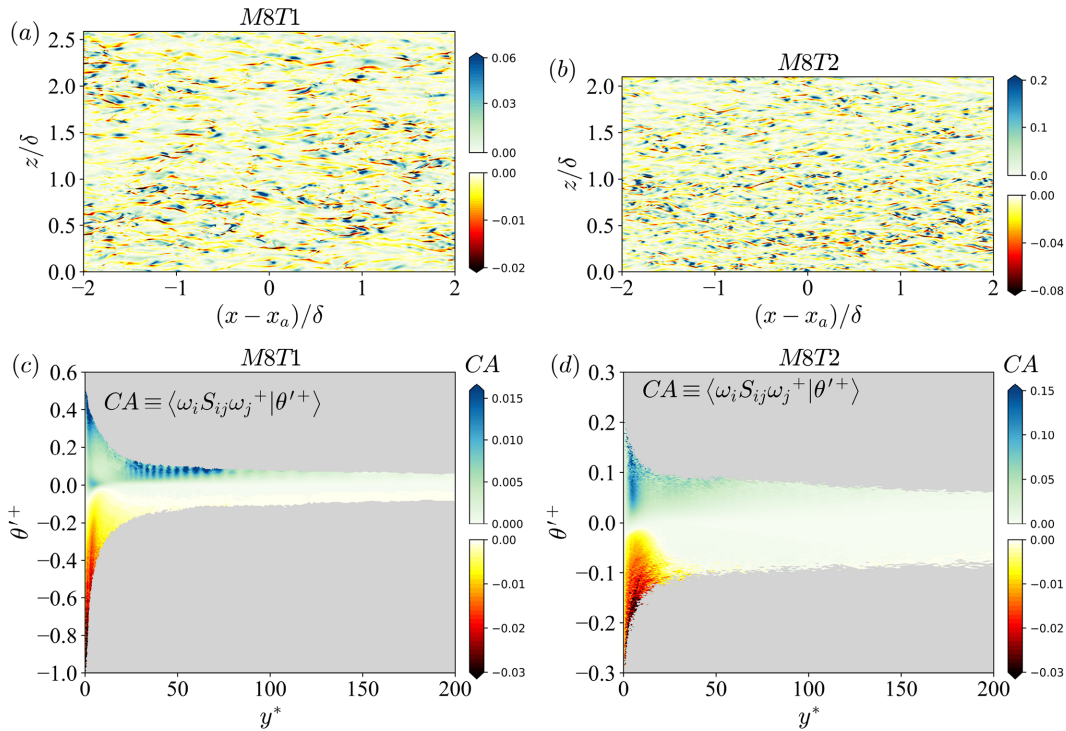
FIG. 7. (a) and (b): The contour of the normalized enstrophy production $\omega_i S_{ij} \omega_j{}^+$ at $y^* = 8$ in (a) M8T1 and (b) M8T2. (c) and (d): The streamwise-spanwise averages of the normalized enstrophy production $\omega_i S_{ij} \omega_j{}^+$ conditioned on the normalized fluctuating velocity divergence θ'^+ along wall-normal direction y^* in (c) M8T1 and (d) M8T2.

production structures are much fatter, mainly due to the preference to be located in the expansion region.

The averages of the normalized enstrophy production $\omega_i S_{ij} \omega_j{}^+_{(k)}$ contributed by various flow topologies $S^{(k)}$ conditioned on the normalized fluctuating velocity divergence θ'^+ at $y^* = 8$ are plotted in Fig. 8. It is noted that the variations of $\langle \omega_i S_{ij} \omega_j{}^+_{(k)} | \theta'^+ \rangle$ along with the local normalized fluctuating velocity divergence θ'^+ are similar among different wall-normal locations near the wall, and the conditional averages $\langle \omega_i S_{ij} \omega_j{}^+_{(k)} | \theta'^+ \rangle$ at $y^* = 8$ are shown as representative. The averages of the normalized enstrophy production $\omega_i S_{ij} \omega_j{}^+_{(k)}$ contributed by flow topologies $S^{(1)}$, $S^{(3)}$, $S^{(4)}$, and $S^{(5)}$ exhibit negative values in the compression region. Moreover, the averages of the normalized enstrophy production $\omega_i S_{ij} \omega_j{}^+_{(k)}$ contributed by flow topologies $S^{(1)}$, $S^{(2)}$, $S^{(4)}$, $S^{(7)}$, and $S^{(8)}$ are positive in the expansion region. It is found that the wall temperature has significant influence on $\langle \omega_i S_{ij} \omega_j{}^+_{(k)} | \theta'^+ \rangle$. The intensities of the averages of normalized enstrophy production $\omega_i S_{ij} \omega_j{}^+_{(k)}$ contributed by flow topologies $S^{(3)}$ and $S^{(5)}$ in the compression region are significantly enhanced by the colder wall temperature, leading to the main contributions to the enstrophy destruction by flow topologies $S^{(3)}$ and $S^{(5)}$ in M8T1. Furthermore, the intensities of the average of the normalized enstrophy production $\omega_i S_{ij} \omega_j{}^+_{(k)}$ contributed by flow topologies $S^{(1)}$ and $S^{(4)}$ are largely suppressed and that contributed by flow topology $S^{(7)}$ is significantly enhanced in the expansion region with colder wall temperature, giving rise to the different observations that flow topology $S^{(7)}$ is the major

contribution to the enstrophy production in M8T1, while flow topologies $S^{(1)}$ and $S^{(4)}$ play the main role in the enstrophy production in M8T2 in the expansion region. Overall, it is found that the enstrophy destruction is mainly located in the compression region and generated by the non-swirling, straining structure with two contracting directions and the compressive vortical structure with an out-of-plane contracting strain. On the contrary, the enstrophy production is mainly located in the expansion region, where the expansive vortical structures with an out-of-plane stretching strain are concentrated. The contributions of topologies $S^{(1)}$, $S^{(2)}$, and $S^{(4)}$ to the enstrophy production are mainly gathered in weak expansion region. These statistical observations are consistent with the instantaneous flow contours shown in Figs. 7(a) and 7(b).

The streamwise-spanwise averages of the normalized fluctuating enstrophy production $\omega_i' S_{ij}' \omega_j'^+$ and its solenoidal and dilatational components along wall-normal direction in M8T015 and M8T08 are plotted in Fig. 9. The positive solenoidal component $\langle \omega_i' S_{s,ij}' \omega_j'^+ \rangle_{xz}$ is dominant in positive $\langle \omega_i' S_{ij}' \omega_j'^+ \rangle_{xz}$ across the boundary layer, indicating that the fluctuating enstrophy production is predominant over the fluctuating enstrophy destruction, and the mean fluctuating enstrophy production term is mainly governed by its solenoidal component. However, the dilatational component $\langle \omega_i' S_{d,ij}' \omega_j'^+ \rangle_{xz}$ only has significant contribution near the wall, and the relative contribution of $\langle \omega_i' S_{d,ij}' \omega_j'^+ \rangle_{xz}$ in M8T015 is much larger than that in M8T08, due to stronger compressibility with cold wall temperature in the near wall region.[4,32,33] Moreover, $\langle \omega_i' S_{d,ij}' \omega_j'^+ \rangle_{xz}$ in M8T015 exhibits strong mean enstrophy destruction, while that in M8T08 reveals a weak mean enstrophy production near the wall, which implies that the cold
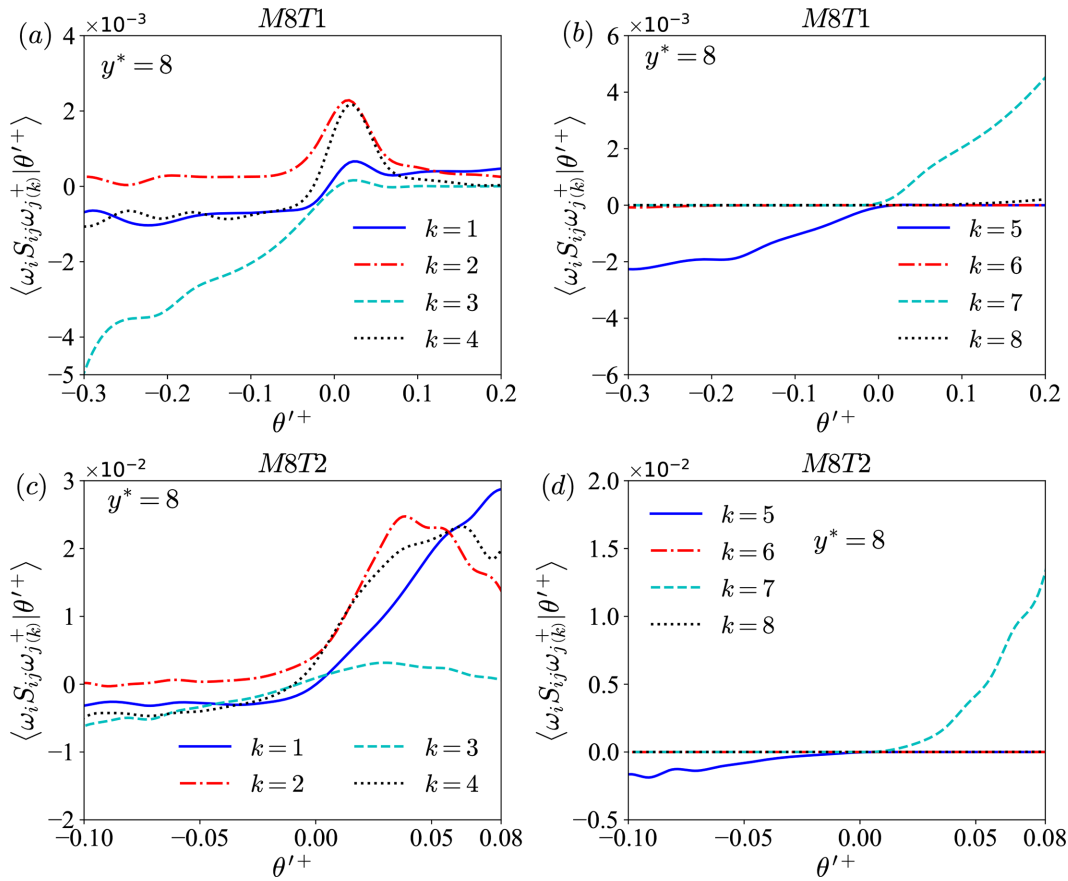
FIG. 8. The averages of the normalized enstrophy production $\omega_i S_{ij} \omega_j^+{}_{(k)}$ contributed by various flow topologies $S^{(k)}$ conditioned on the normalized fluctuating velocity divergence θ'^+ at $y^* = 8$ in (a) M8T1 with $k = 1 - 4$, (b) M8T1 with $k = 5 - 8$; and (c) M8T2 with $k = 1 - 4$, and (d) M8T2 with $k = 5 - 8$.

wall temperature significantly enhances the local fluctuating enstrophy destruction near the wall.

The average of the normalized fluctuating enstrophy production $\omega_i' S_{ij}' \omega_j'^+$ contributed by various flow topologies $S'^{(k)}$ conditioned on

the normalized fluctuating velocity divergence θ'^+ at $y^* = 8$ is plotted in Fig. 10. In the compression region, as the magnitude of the normalized fluctuating velocity divergence increases, the magnitudes of $\langle \omega_i' S_{ij}' \omega_j'^+ | \theta'^+ \rangle$ contributed by flow topologies $S'^{(1)}$, $S'^{(3)}$, $S'^{(4)}$,
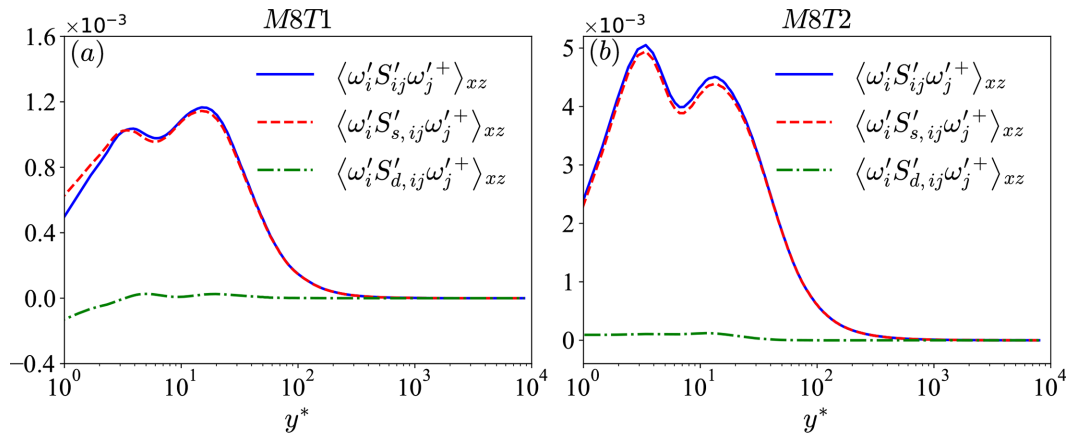

FIG. 9. The streamwise-spanwise averages of the normalized fluctuating enstrophy production $\omega_i' S_{ij}' \omega_j'^+$ and its solenoidal and dilatational components along wall-normal direction in (a) M8T015 and (b) M8T08.
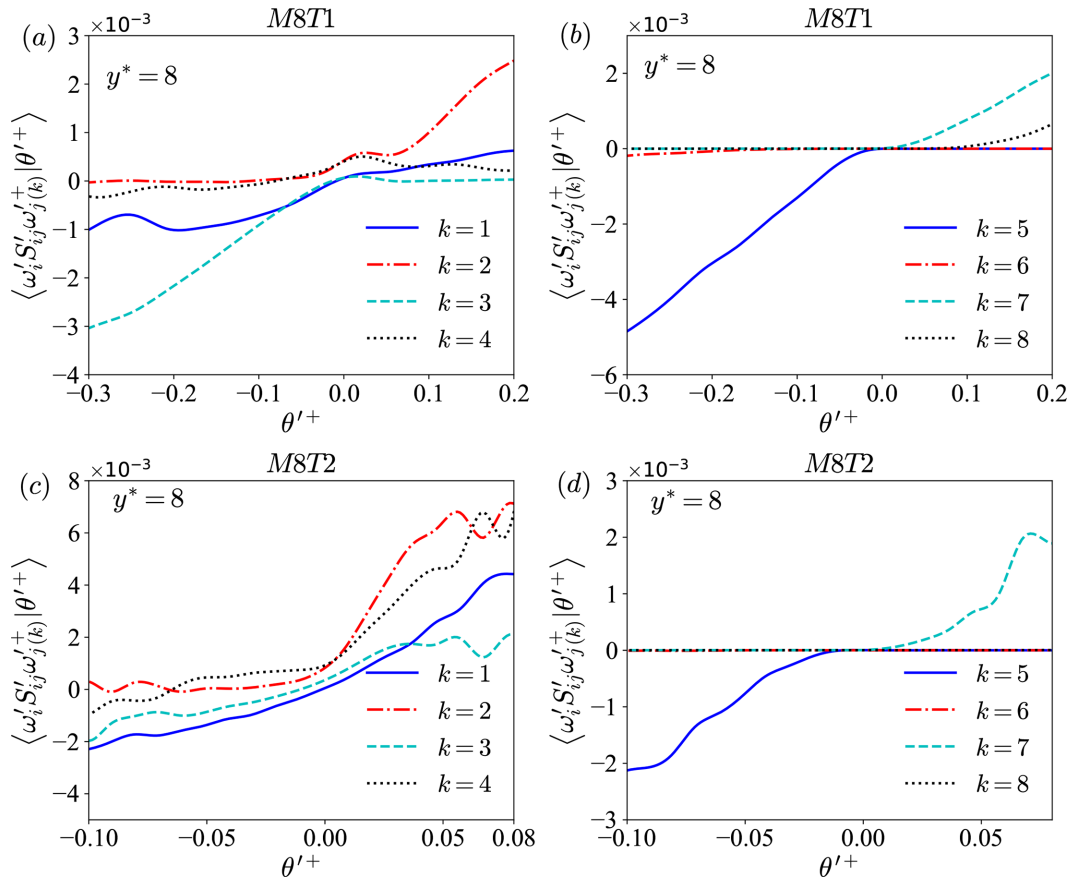
FIG. 10. The average of the normalized fluctuating enstrophy production $\omega_i' S_{ij}' \omega_{j(k)}'^+$ contributed by various flow topologies $S'^{(k)}$ conditioned on the normalized fluctuating velocity divergence θ'^+ at $y^* = 8$ in (a) M8T1 with $k = 1 - 4$, (b) M8T1 with $k = 5 - 8$; and (c) M8T2 with $k = 1 - 4$, (d) M8T2 with $k = 5 - 8$.

and $S^{(5)}$ increase and have significant contributions to the fluctuating enstrophy destruction. While in the expansion region, as the normalized fluctuating velocity divergence increases, $\langle \omega_i' S_{ij}' \omega_{j(k)}'^+ | \theta'^+ \rangle$ contributed by flow topologies $S'^{(1)}$, $S'^{(2)}$, $S'^{(7)}$, and $S'^{(8)}$ increase and give rise to the fluctuating enstrophy production. Furthermore, the wall temperature has the important effect on $\langle \omega_i' S_{ij}' \omega_{j(k)}'^+ | \theta'^+ \rangle$. In the compression region, the intensities of $\langle \omega_i' S_{ij}' \omega_{j(k)}'^+ | \theta'^+ \rangle$ contributed by flow topologies $S'^{(3)}$ and $S'^{(5)}$ are significantly enhanced by the colder wall temperature. However, in the expansion region, the intensities of $\langle \omega_i' S_{ij}' \omega_{j(k)}'^+ | \theta'^+ \rangle$ contributed by flow topologies $S'^{(1)}$ and $S'^{(4)}$ are suppressed and that contributed by flow topology $S'^{(7)}$ is enhanced by the colder wall temperature.

C. Statistics of eigenvalues and eigenvectors of the strain rate tensor

It is well known that the enstrophy production plays a significant role in the vortex evolution dynamics; thus, it should pay special attention to figure out the properties of the enstrophy production. The eigenvalue decomposition of the strain rate tensor can be applied to investigate the mechanism of the enstrophy production. The enstrophy production $\omega_i S_{ij} \omega_j$ can be expressed in terms of the eigenvalues of

the strain rate tensor and the cosines of angles between vorticity and the eigenvectors[23,30]

$$\omega_i S_{ij} \omega_j = \omega^2 [\lambda_{1,S} \cos^2(\omega, \Lambda_{1,S}) + \lambda_{2,S} \cos^2(\omega, \Lambda_{2,S}) + \lambda_{3,S} \cos^2(\omega, \Lambda_{3,S})]. \quad (20)$$

Here, we denote three eigenvectors of the strain rate tensor S_{ij} as $\Lambda_{1,S}$, $\Lambda_{2,S}$, and $\Lambda_{3,S}$, with corresponding eigenvalues $\lambda_{1,S}$, $\lambda_{2,S}$, and $\lambda_{3,S}$ arranged in ascending order, i.e., $\lambda_{1,S} \leq \lambda_{2,S} \leq \lambda_{3,S}$. The normalized eigenvalues of the strain rate tensor are defined as

$$\beta_{j,S} = \frac{\lambda_{j,S}}{\sqrt{\lambda_{1,S}^2 + \lambda_{2,S}^2 + \lambda_{3,S}^2}}. \quad (21)$$

The cosines of angles between vorticity and eigenvectors of the strain rate tensor are defined as $\phi_{j,S} = \cos(\omega, \Lambda_{j,S})$.

Similarly, three eigenvectors of the fluctuating strain rate tensor S_{ij}' are written as $\Lambda_{1,S'}$, $\Lambda_{2,S'}$, and $\Lambda_{3,S'}$, with corresponding eigenvalues $\lambda_{1,S'}$, $\lambda_{2,S'}$, and $\lambda_{3,S'}$ arranged in ascending order, i.e., $\lambda_{1,S'} \leq \lambda_{2,S'} \leq \lambda_{3,S'}$. The normalized eigenvalues of the fluctuating strain rate tensor are defined as

$$\beta_{j,S'} = \frac{\lambda_{j,S'}}{\sqrt{\lambda_{1,S'}^2 + \lambda_{2,S'}^2 + \lambda_{3,S'}^2}}. \quad (22)$$

The cosines of angles between fluctuating vorticity and eigenvectors of the fluctuating strain rate tensor are defined as $\phi_{j,S'} = \cos(\omega', \Lambda_{j,S'})$.

Three eigenvectors of the solenoidal component of fluctuating strain rate tensor $S'_{s,ij}$ are written as Λ_{1,S'_s}, Λ_{2,S'_s}, and Λ_{3,S'_s}, with corresponding eigenvalues λ_{1,S'_s}, λ_{2,S'_s}, and λ_{3,S'_s} arranged in ascending order, i.e., $\lambda_{1,S'_s} \leq \lambda_{2,S'_s} \leq \lambda_{3,S'_s}$. The normalized eigenvalues of the solenoidal component of fluctuating strain rate tensor are defined as

$$\beta_{j,S'_s} = \frac{\lambda_{j,S'_s}}{\sqrt{\lambda_{1,S'_s}^2 + \lambda_{2,S'_s}^2 + \lambda_{3,S'_s}^2}}. \quad (23)$$

The cosines of angles between fluctuating vorticity and eigenvectors of the solenoidal component of fluctuating strain rate tensor are defined as $\phi_{j,S'_s} = \cos(\omega', \Lambda_{j,S'_s})$.

Three eigenvectors of the dilatational component of fluctuating strain rate tensor $S'_{d,ij}$ are written as Λ_{1,S'_d}, Λ_{2,S'_d}, and Λ_{3,S'_d}, with

corresponding eigenvalues λ_{1,S'_d}, λ_{2,S'_d}, and λ_{3,S'_d} arranged in ascending order, i.e., $\lambda_{1,S'_d} \leq \lambda_{2,S'_d} \leq \lambda_{3,S'_d}$. The normalized eigenvalues of the dilatational component of fluctuating strain rate tensor are defined as

$$\beta_{j,S'_d} = \frac{\lambda_{j,S'_d}}{\sqrt{\lambda_{1,S'_d}^2 + \lambda_{2,S'_d}^2 + \lambda_{3,S'_d}^2}}. \quad (24)$$

The cosines of angles between fluctuating vorticity and eigenvectors of the dilatational component of fluctuating strain rate tensor are defined as $\phi_{j,S'_d} = \cos(\omega', \Lambda_{j,S'_d})$. Accordingly, in order to understand the mechanism of the enstrophy production, the eigenvalues of the strain rate tensor and the alignment between the vorticity vector and the eigenvectors of the strain rate tensor are the most important quantities to be investigated.

PDFs of the normalized eigenvalues $\beta_{j,S'}$ of the fluctuating strain rate tensor in M8T1 and M8T2 are plotted in Figs. 11(a), 11(d), and
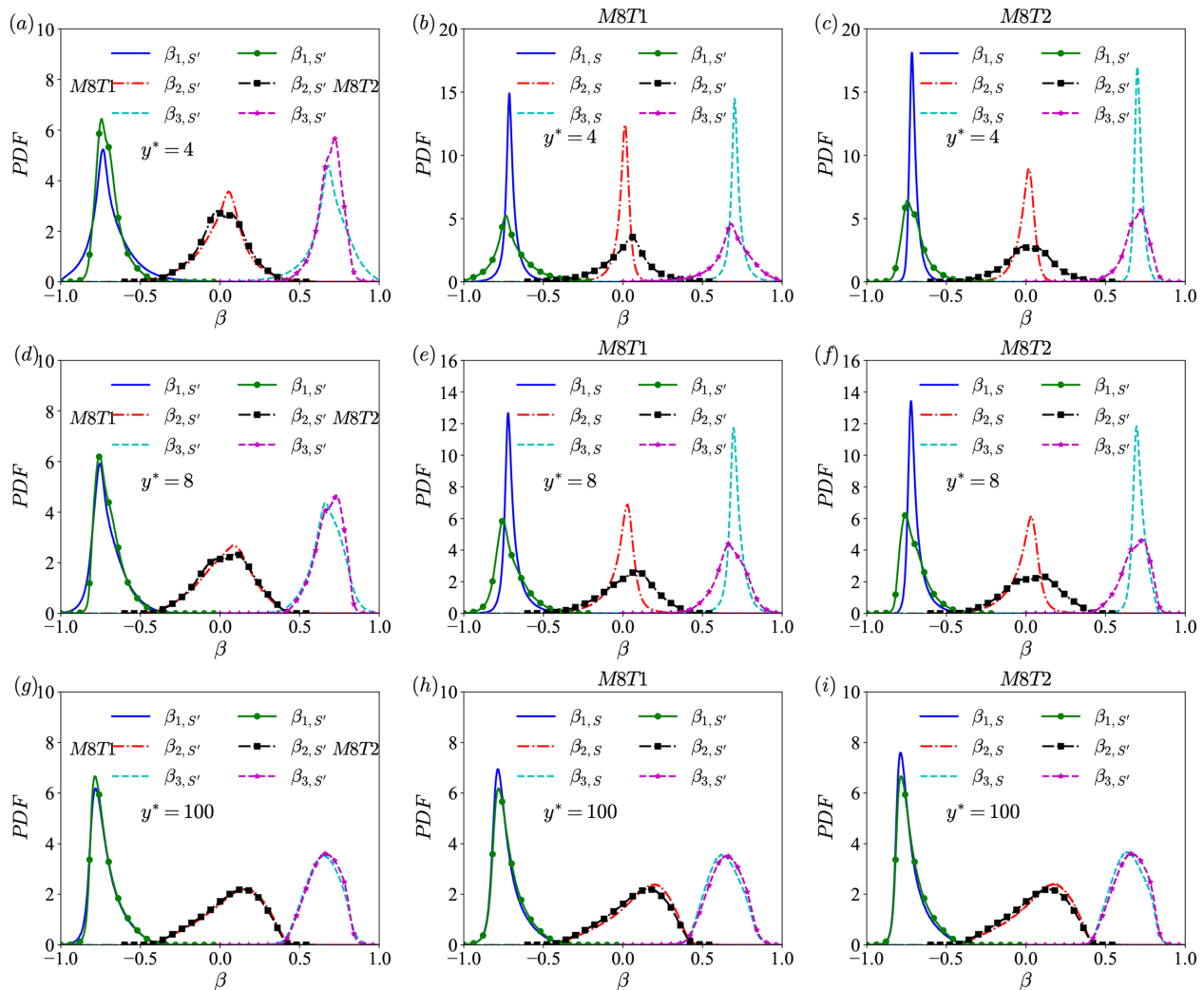

FIG. 11. (a), (d), and (g): PDFs of the normalized eigenvalues $\beta_{j,S'}$ of the fluctuating strain rate tensor in M8T1 and M8T2 at (a) $y^* = 4$, (d) $y^* = 8$, and (g) $y^* = 100$. The lines represent PDFs of $\beta_{j,S'}$ in M8T1, and the lines with markers represent PDFs of $\beta_{j,S'}$ in M8T2. (b), (e), and (h): PDFs of the normalized eigenvalues $\beta_{j,S}$ and $\beta_{j,S'}$ in M8T1 at (b) $y^* = 4$, (e) $y^* = 8$, and (h) $y^* = 100$. (c), (f), and (i): PDFs of the normalized eigenvalues $\beta_{j,S}$ and $\beta_{j,S'}$ in M8T2 at (c) $y^* = 4$, (f) $y^* = 8$, and (i) $y^* = 100$.

11(g). It is found that in the near wall region ($y^* = 4$) where the compressibility effect is strong, the effect of wall temperature on the distributions of $\beta_{j,S'}$ is prominent. Particularly, the shapes of PDFs of $\beta_{1,S'}$ and $\beta_{3,S'}$ become wider, while the shape of PDF of $\beta_{2,S'}$ becomes thinner with colder wall temperature. As the wall-normal distance increases, the differences of PDFs of $\beta_{j,S'}$ between M8T1 and M8T2 become smaller. In the far-wall region ($y^* = 100$) where compressibility effect is weak, PDFs of $\beta_{j,S'}$ in M8T1 and M8T2 are nearly coincident, indicating that the effect of wall temperature on the distributions of $\beta_{j,S'}$ is mainly concentrated in the near wall region. Moreover, the peak locations of PDFs of $\beta_{j,S'}$ in M8T1 and M8T2 are similar far from the wall. It is also found that PDFs of eigenvalues of $\beta_{j,S'}$ in the near wall region are much thinner than those in the far wall region, mainly due to the strong wall effect. PDFs of the normalized eigenvalues $\beta_{j,S}$ and $\beta_{j,S'}$ in M8T1 are shown in Figs. 11(b), 11(e), and 11(h), and those in M8T2 are shown in Figs. 11(c), 11(f), and 11(i). It is found that PDFs of $\beta_{j,S}$ are much thinner than those of $\beta_{j,S'}$ near the wall, mainly resulting from the strong mean shear near the wall. In the far wall region ($y^* = 100$) where the mean shear is weak, PDFs of $\beta_{j,S}$ and $\beta_{j,S'}$ become more similar compared with those in the near wall region. It is worth noting that the most probable eigenvalue ratio for the fluctuating strain rate tensor S'_{ij} far from the wall is nearly $(-4:1:3)$, which is similar to the observations in incompressible turbulence[42] and weakly compressible turbulence.[41,43] However, the most probable eigenvalue ratio of the fluctuating strain rate tensor S'_{ij} in the near-wall region is very close to $(-1:0:1)$.

The averages of the normalized eigenvalues $\beta_{j,S}$ along the wall-normal direction are shown in Fig. 12(a). It is shown that the average of $\beta_{j,S}$ is unchangeable in the near wall region and far wall region, except for a slight variation in the buffer layer. Moreover, the average values of the normalized eigenvalues $\beta_{j,S}$ in both cases are similar in the near wall region and far wall region.

The averages of the cosines of the angle between vorticity and eigenvectors $\phi_{j,S}$ along the wall-normal direction are shown in Fig. 12(b). It is found that in the near wall region, the direction of vorticity is almost coincident with that of the intermediate eigenvector, while the direction of vorticity is nearly perpendicular to the first and third eigenvectors. As the wall-normal distance increases, the above strong tendency becomes weaker. The averages of the contributions $\omega^2 \lambda_{k,S} \cos^2(\omega, \Lambda_{k,S}) / \langle \omega_i S_{ij} \omega_j \rangle$ along the wall-normal direction are plotted in Fig. 12(c). It is illustrated that in the near wall region, the

enstrophy production is mainly contributed by its intermediate eigenvalue, and the contributions of the first and third eigenvalues are almost negligible. As the wall-normal distance increases, the contribution of the intermediate eigenvalue becomes smaller, and the contribution of the third eigenvalue to the enstrophy production drastically increases, leading to the strong contributions of both the intermediate and third eigenvalues to the positive enstrophy production far from the wall. Furthermore, the enstrophy destruction is mainly governed by the first eigenvalue.

The PDFs and conditional PDFs of the normalized eigenvalues of the strain rate tensor S_{ij} at $y^+ = 8$ (buffer layer) and $y^+ = 100$ (logarithmic layer) in M8T1 are plotted in Fig. 13. The legends represent the conditional range of the normalized fluctuating velocity divergence θ'^+. It is found that the peak values of the conditional PDFs of $\beta_{1,S}$, $\beta_{2,S}$, and $\beta_{3,S}$ shift to the left side as the compression level increases, and shift to the right side as the expansion level increases. Furthermore, the shapes of the conditional PDFs at $y^+ = 8$ (buffer layer) are much thinner than those at $y^+ = 100$ (logarithmic layer), probably due to the strong wall effect and the strong mean shear. Accordingly, it is concluded that in the strong compression region, more sheet-like shocklets appear, which lead to the peak values of the conditional PDFs of $\beta_{j,S}$ shifting to the left side. On the other hand, in the strong expansion region, the local expansion motions act as the blob-like structures, which give rise to the peak values of the conditional PDFs of $\beta_{j,S}$ shifting to the right side.

The PDF and conditional PDFs of the normalized eigenvalue β_{1,S'_s} at $y^+ = 8$ (buffer layer) in M8T1 are plotted in Fig. 14(a). It is found that the PDF shapes of β_{1,S'_s} are nearly unchanged by the local fluctuating velocity divergence, except that the strong compression and expansion motions slightly broaden the PDF shapes. The PDF shapes of β_{2,S'_s} and β_{3,S'_s} (not reported here) are also nearly unchanged by the local fluctuating velocity divergence, indicating that the local compressibility has negligible influence on the solenoidal component of fluctuating strain rate tensor, which is consistent with the observation in compressible isotropic turbulence.[23] The PDFs and conditional PDFs of the normalized eigenvalues β_{j,S'_d} at $y^+ = 8$ (buffer layer) in M8T1 are plotted in Figs. 14(b)–14(d). It is shown that in the compression regions, the most probable value of β_{1,S'_d} decreases toward to -1 as the magnitude of the fluctuating velocity divergence increases. However, in the expansion regions, the most probable value of β_{3,S'_d} increases toward to 1 as the magnitude of the fluctuating velocity divergence increases.
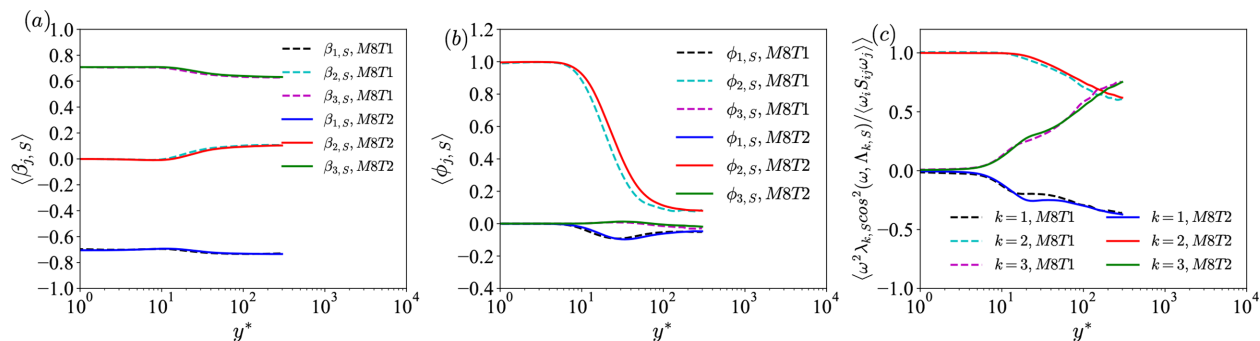

FIG. 12. (a) The averages of the normalized eigenvalues $\beta_{j,S}$ along the wall-normal direction in M8T1 and M8T2. (b) The averages of the cosines of the angle between vorticity and eigenvectors $\phi_{j,S}$ along the wall-normal direction in M8T1 and M8T2. (c) The averages of the contributions $\omega^2 \lambda_{k,S} \cos^2(\omega, \Lambda_{k,S}) / \langle \omega_i S_{ij} \omega_j \rangle$ along the wall-normal direction in M8T1 and M8T2.
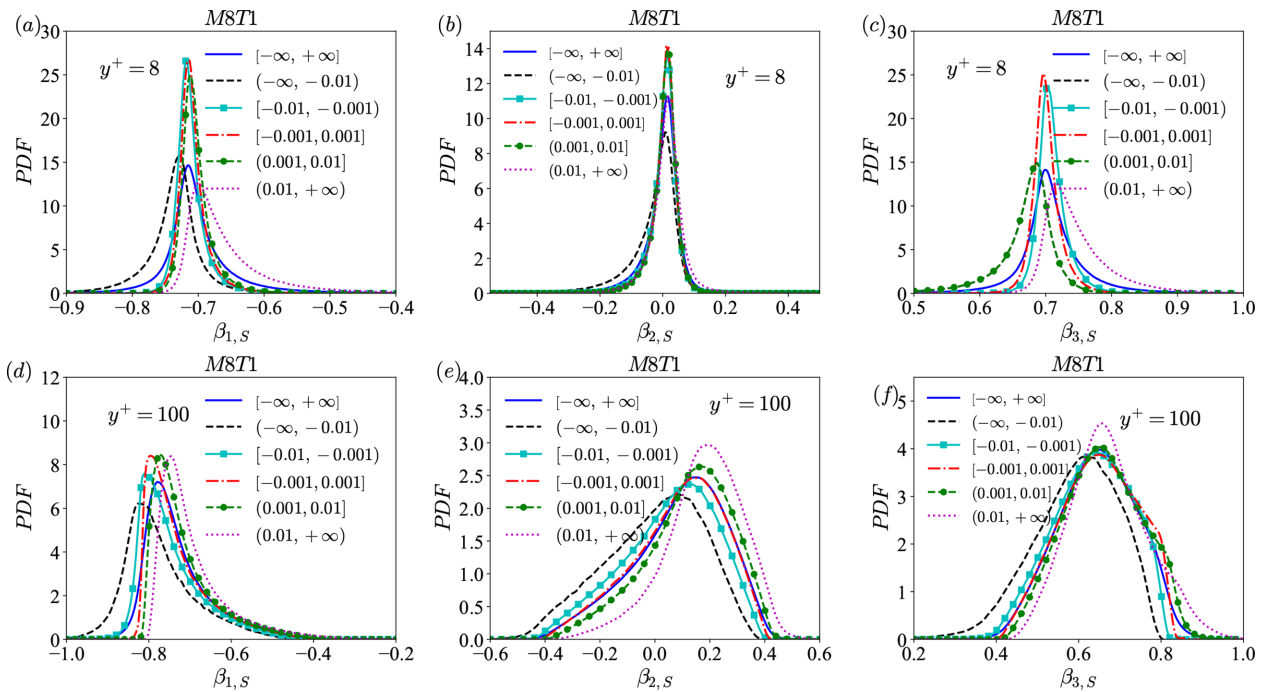
FIG. 13. (a) and (d): The PDFs and conditional PDFs of the normalized eigenvalue $\beta_{1,S}$ of the strain rate tensor S_{ij} at (a) $y^+ = 8$ (buffer layer) and (d) $y^+ = 100$ (logarithmic layer) in M8T1. (b) and (e): The PDFs and conditional PDFs of the normalized eigenvalue $\beta_{2,S}$ of the strain rate tensor S_{ij} at (b) $y^+ = 8$ (buffer layer) and (e) $y^+ = 100$ (logarithmic layer) in M8T1. (c) and (f): The PDFs and conditional PDFs of the normalized eigenvalue $\beta_{3,S}$ of the strain rate tensor S_{ij} at (c) $y^+ = 8$ (buffer layer) and (f) $y^+ = 100$ (logarithmic layer) in M8T1. The legends represent the conditional range of the normalized fluctuating velocity divergence θ'^+.

The PDFs and conditional PDFs of the cosines of the angle between vorticity and eigenvectors $\phi_{j,S}$ at $y^+ = 8$ (buffer layer) and $y^+ = 100$ (logarithmic layer) are shown in Fig. 15. It is shown that there is a strong tendency for the vorticity to align with the intermediate eigenvector both in buffer layer and logarithmic layer. In Fig. 16, the peak locations of the PDFs of the cosines of the angle between vorticity and the positive z-axis (0,0,1) as well as the angle between the intermediate eigenvector and the positive z-axis (0,0,1) are very close to -1, indicating that the directions of both the vorticity and the intermediate eigenvector are almost along the negative z-axis $(0,0,-1)$. Furthermore, the most probable angle between the first eigenvector and the positive x-axis (1,0,0) is almost $\pi/4$, and the most probable angles between the third eigenvector and the positive x-axis (1,0,0) are $-\pi/4$ and $3\pi/4$, respectively. The above observations reveal that the flow pattern of the strain rate tensor S_{ij} is almost an in-plane saddle point locating in the x–y plane. The inclined angle $\pi/4$ is consistent with previous observation in the incompressible turbulent channel flow.[16] The above observations are coincident with the "attached eddy" model proposed by Townsend:[44] the vortices originate in the buffer layer and leave two legs in this region, and then the two legs protrude to the wall inclined at an angle of $\pi/4$. Moreover, there is a relatively strong tendency for vorticity to be perpendicular to the first eigenvector (the one with the most negative eigenvalue) as well as the third eigenvector (the one with the most positive eigenvalue) in the buffer layer mainly due to the strong wall effect. However, the tendency for vorticity to be perpendicular to the first eigenvector becomes weaker, and the distribution of the angle between the vorticity and the third eigenvector

becomes approximately uniform in the logarithmic layer. The behavior of the distributions of the cosines of the angles between vorticity and eigenvectors in the logarithmic layer is similar to the observations in the incompressible turbulence,[42,45,46] weakly compressible turbulence[41,43] and highly compressible isotropic turbulence.[23]

Furthermore, the influence of the fluctuating velocity divergence on the angles between vorticity and eigenvectors is also investigated. It is shown in Fig. 15 that both the positive and negative values of the fluctuating velocity divergence weaken the nearly perpendicular alignment with vorticity for the first and third eigenvector and also weaken the parallel alignment with vorticity for the intermediate eigenvector in the buffer layer. However, in the logarithmic layer, the effect of fluctuating velocity divergence drastically changes. The compression motions weaken the perpendicular alignment with vorticity for the first eigenvector and also weaken the parallel alignment with vorticity for the intermediate eigenvector. On the contrary, the expansion motions strengthen the perpendicular alignment with vorticity for the first eigenvector and the parallel alignment with vorticity for the intermediate eigenvector. Furthermore, the negative fluctuating velocity divergence strengthens the tendency of the distribution of the angle between the vorticity and the third eigenvector to be uniform, while the positive fluctuating velocity divergence makes the third eigenvector to be more perpendicular to the vorticity. The different behaviors of the effect of the local fluctuating velocity divergence on the angles between vorticity and eigenvectors in the buffer layer and the logarithmic layer are mainly due to the different structures of the
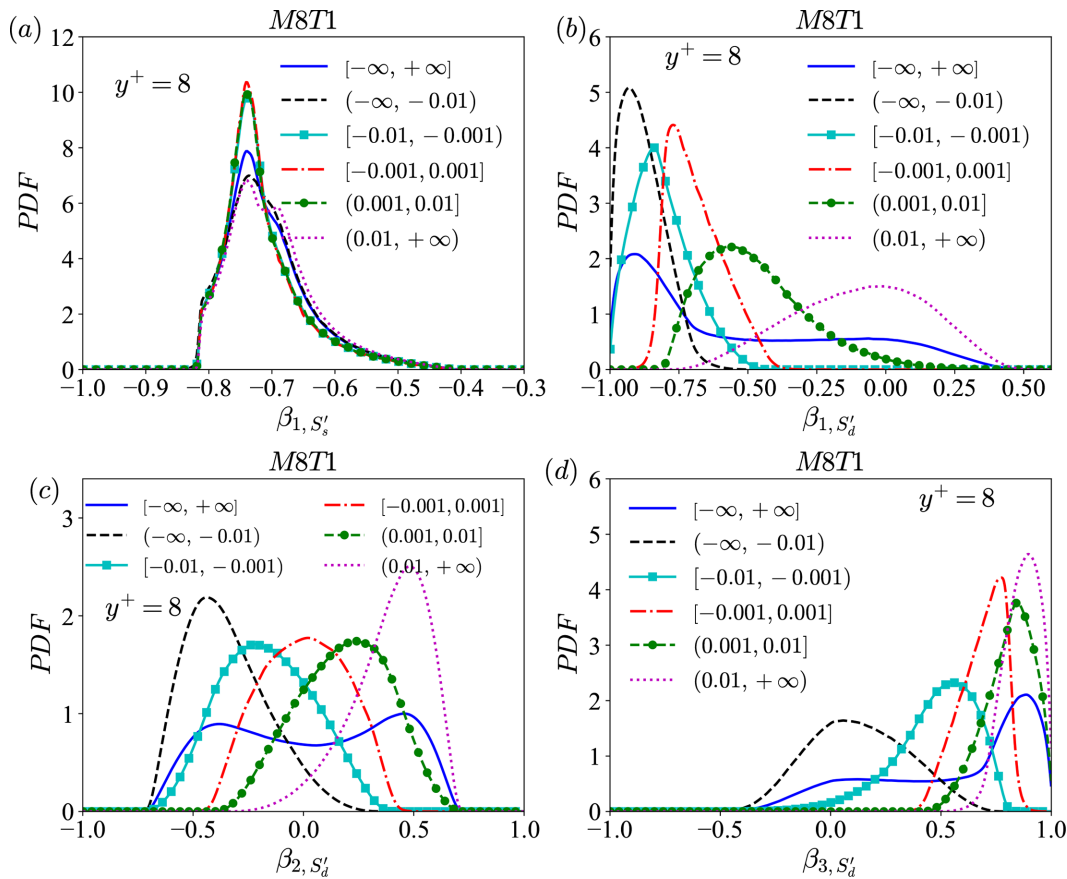
FIG. 14. (a) The PDF and conditional PDFs of the normalized eigenvalue β_{1,S'_s} of the solenoidal component of fluctuating strain rate tensor at $y^+ = 8$ (buffer layer) in M8T1. (b)–(d): The PDFs and conditional PDFs of the normalized eigenvalues β_{j,S'_d} of the dilatational component of fluctuating strain rate tensor at $y^+ = 8$ (buffer layer) in M8T1. The legends represent the conditional range of the normalized fluctuating velocity divergence θ'^+.

compression and expansion motions in different regions. In the buffer layer, the compression and expansion motions exhibit the sheet-like structures due to the strong wall effect. While in the logarithmic layer, the compression motions exhibit the sheet-like structures, and the expansion motions show the blob-like structures.

The average values of $\beta_{j,S}$, β_{j,S'_s}, and β_{j,S'_d} conditioned on the normalized fluctuating velocity divergence θ'^+ in M8T1 are plotted in Fig. 17. The conditional averages $\langle \beta_{k,S}|\theta'^+ \rangle$, $\langle \beta_{k,S'_s}|\theta'^+ \rangle$, and $\langle \beta_{k,S'_d}|\theta'^+ \rangle$ in M8T2 have similar trends compared with those in M8T1, which are omitted here. It is found that both in the buffer layer and logarithmic layer, the magnitude of the conditional average of the first eigenvalue $\beta_{1,S}$ decreases rapidly, while the conditional average of the third eigenvalue $\beta_{3,S}$ increases sharply as the fluctuating velocity divergence increases from the strong compression region to strong expansion region. The intermediate eigenvalue $\beta_{2,S}$ is found to be pretty small, but is significant in determining the enstrophy production by vortex stretching. It is proved by Betchov[47] that the positive value of the intermediate eigenvalue of the strain rate tensor is necessary for the enstrophy production term to produce enstrophy in the incompressible flow. It is found that the conditional average of the intermediate eigenvalue $\beta_{2,S}$ increases from negative to positive as the

fluctuating velocity divergence increases. The zero crossing occurs at nearly $\theta'^+ \approx 0$, which is consistent with the location where the conditional average of $\omega_i S_{ij} \omega_j$ changes from destruction to production.

After the Helmholtz decomposition, the fluctuating velocity divergence has negligible influence on the conditional averages of β_{1,S'_s}, β_{2,S'_s}, and β_{3,S'_s} in the buffer layer and logarithmic layer. For the dilatational component, the conditional average of β_{j,S'_d} is nearly unchanged in strong compression and expansion regions, and the values of the conditional average of β_{j,S'_d} increase sharply as the fluctuating velocity divergence changes from the weak compression region to the weak expansion region.

Figure 18 shows the conditional averages of the enstrophy production by the three eigenvectors of the strain rate tensor $\Lambda_{j,S}$. The data for the large magnitude of the normalized fluctuating velocity divergence are quite scattered due to lack of samples. It is found that for the compression region $\theta'^+ < 0$, the magnitudes of the conditional average of $\omega^2 \lambda_{k,S} \cos^2(\omega, \Lambda_{k,S})$ increase sharply as the magnitude of the fluctuating velocity divergence increases. Furthermore, for the expansion region $\theta'^+ > 0$, the magnitudes of the conditional average of $\omega^2 \lambda_{k,S} \cos^2(\omega, \Lambda_{k,S})$ increase drastically as the fluctuating velocity divergence becomes larger. It is worth noting that the negative values in the
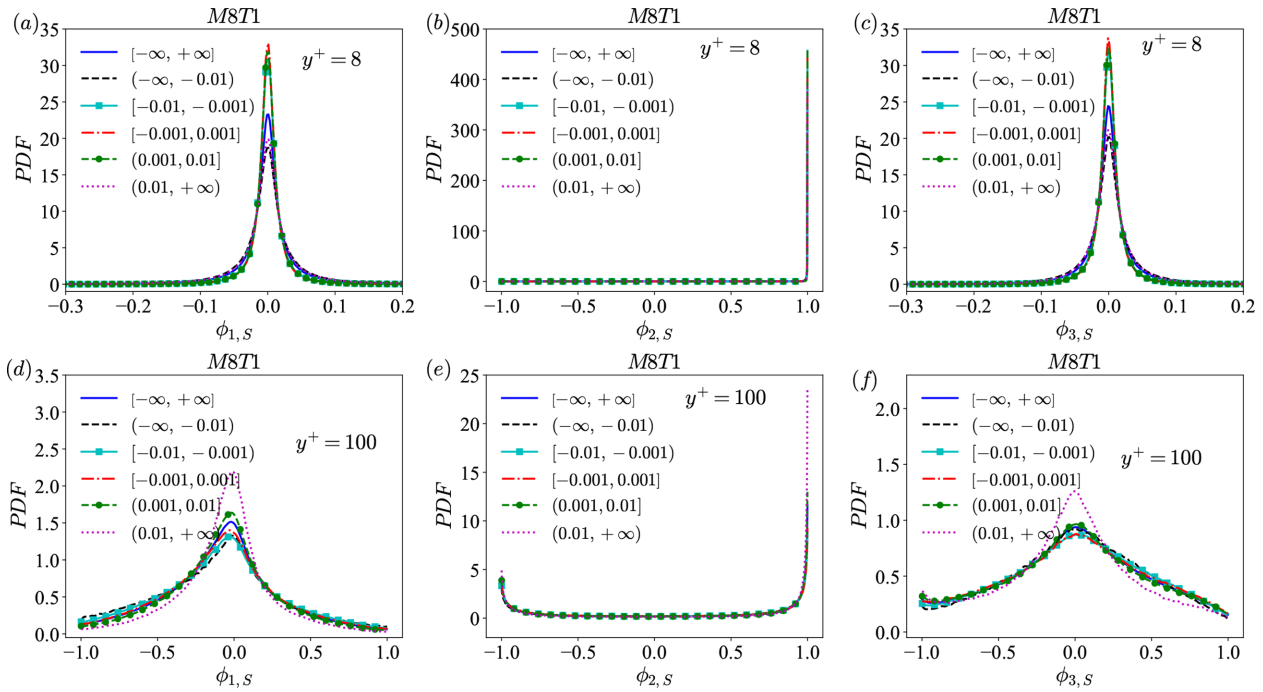
FIG. 15. (a) and (d): The PDFs and conditional PDFs of the cosine of the angle between vorticity and eigenvectors $\phi_{1,S}$ at (a) $y^+ = 8$ (buffer layer) and (d) $y^+ = 100$ (logarithmic layer) in M8T1. (b) and (e): The PDFs and conditional PDFs of the cosine of the angle between vorticity and eigenvectors $\phi_{2,S}$ at (b) $y^+ = 8$ (buffer layer) and (e) $y^+ = 100$ (logarithmic layer) in M8T1. (c) and (f): The PDFs and conditional PDFs of the cosine of the angle between vorticity and eigenvectors $\phi_{3,S}$ at (c) $y^+ = 8$ (buffer layer) and (f) $y^+ = 100$ (logarithmic layer) in M8T1. The legends represent the conditional range of the normalized fluctuating velocity divergence θ'^+.

compression region and the positive values in the expansion region of $\omega_i S_{ij} \omega_j$ are mainly contributed by the second eigenvector $\Lambda_{2,S}$ corresponding to the intermediate eigenvalue $\lambda_{2,S}$ in the buffer layer. However, as the wall-normal location increases, the contribution of the second eigenvector $\Lambda_{2,S}$ to the negative $\omega_i S_{ij} \omega_j$ in the compression region decreases, and the negative values of $\omega_i S_{ij} \omega_j$ in the compression region are primarily contributed by the first eigenvector $\Lambda_{1,S}$ corresponding to the smallest eigenvalue $\lambda_{1,S}$ in the logarithmic layer.

D. Effect of flow topology on the eigenvalues and eigenvectors of the strain rate tensor

PDFs of the normalized eigenvalues $\beta_{j,S}$ of the strain rate tensor for different flow topologies $S^{(k)}$ at $y^+ = 8$ (buffer layer) are plotted in Fig. 19. In the buffer layer, the shapes of PDFs of $\beta_{1,S}$ and $\beta_{3,S}$ of flow topologies $S^{(1)}$ and $S^{(3)}$ are much wider. Furthermore, the most probable value of $\beta_{1,S}$ in the flow topology $S^{(6)}$ corresponding to the compression region is more negative than those in other seven flow
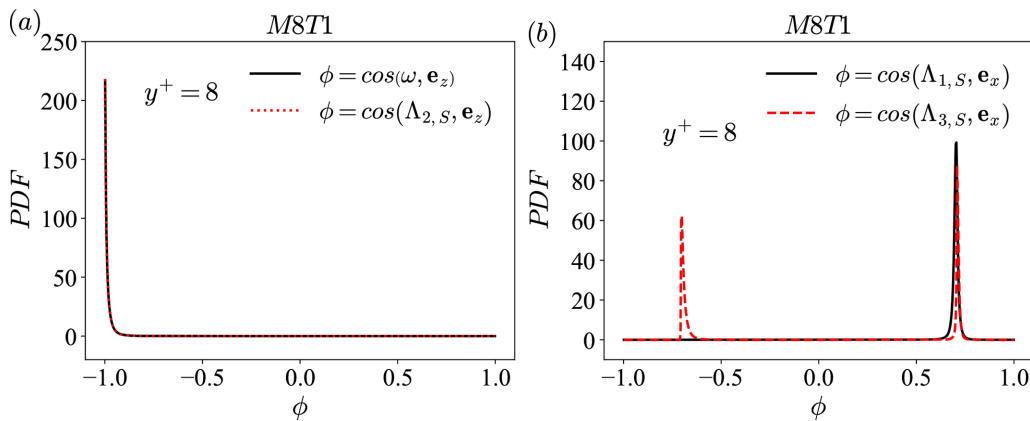

FIG. 16. (a) The PDFs of the cosines of the angle between vorticity and the positive z-axis (0,0,1) as well as the angle between the intermediate eigenvector and the positive z-axis (0,0,1); (b) the PDFs of the cosines of the angle between the first eigenvector and the positive x-axis (1,0,0) as well as the angle between the third eigenvector and the positive x-axis (1,0,0).
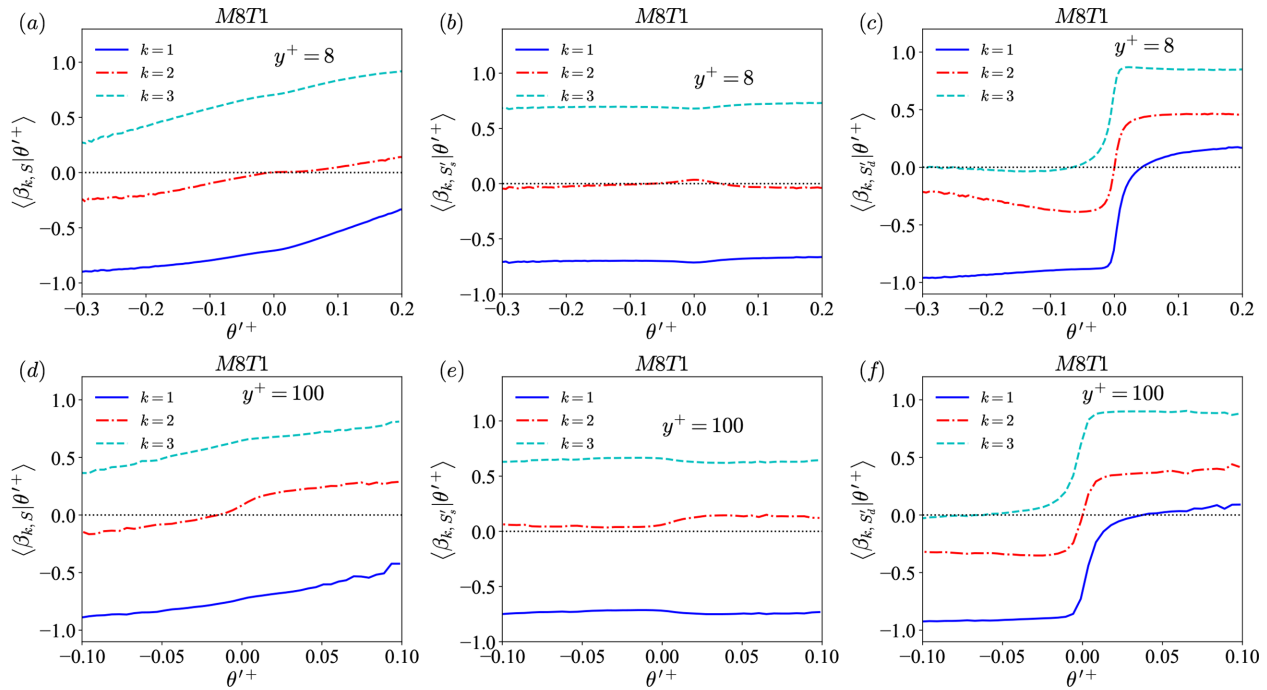
FIG. 17. (a) and (d): The average values of $\beta_{j,S}$ conditioned on the normalized fluctuating velocity divergence θ'^+ at (a) $y^+ = 8$ (buffer layer) and (d) $y^+ = 100$ (logarithmic layer) in M8T1. (b) and (e): The average values of β_{j,S'_s} conditioned on the normalized fluctuating velocity divergence θ'^+ at (b) $y^+ = 8$ (buffer layer) and (e) $y^+ = 100$ (logarithmic layer) in M8T1. (c) and (f): The average values of β_{j,S'_d} conditioned on the normalized fluctuating velocity divergence θ'^+ at (c) $y^+ = 8$ (buffer layer) and (f) $y^+ = 100$ (logarithmic layer) in M8T1.

topologies, while the most probable value of $\beta_{3,S}$ in the flow topology $S^{(8)}$ corresponding to the expansion region is more positive than those in other seven flow topologies. The shape of PDF of $\beta_{2,S}$ in the flow topology $S^{(1)}$ is wide, and the probability of $\beta_{2,S}$ to be negative is slightly larger than that of $\beta_{2,S}$ to be positive in this flow topology. Moreover, the most probable values of $\beta_{2,S}$ in flow topologies $S^{(2)}$, $S^{(4)}$, $S^{(7)}$, and $S^{(8)}$ are positive, while those of $\beta_{2,S}$ in flow topologies $S^{(3)}$, $S^{(5)}$, and $S^{(6)}$ are negative. It can be implied that in the near wall region, the fluid elements with unstable and stretching

characteristics prefer the positive values of $\beta_{2,S}$, which further leads to the enstrophy production. On the other hand, the fluid elements with stable and compressing characteristics are in favor of the negative values of $\beta_{2,S}$, which further gives rise to the enstrophy destruction.

PDFs of the cosines of the angles between vorticity and eigenvectors $\phi_{j,S}$ for different flow topologies $S^{(k)}$ at $y^+ = 8$ (buffer layer) are plotted in Fig. 20 to clarify the effect of flow topology on the alignment between the vorticity and eigenvectors of the strain rate tensor. In the buffer layer, the alignment between the vorticity and the intermediate
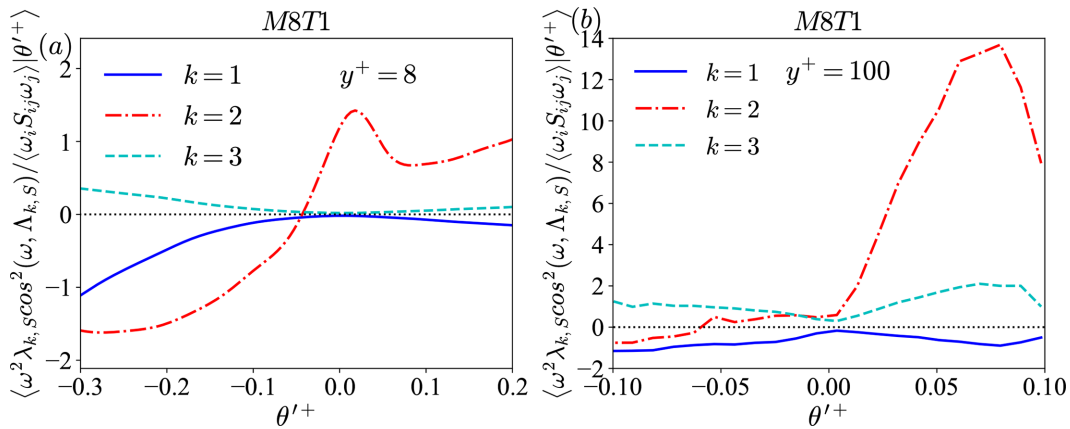

FIG. 18. Conditional averages of the enstrophy production by the three eigenvectors of the strain rate tensor $\Lambda_{j,S}$ at (a) $y^+ = 8$ (buffer layer) and (b) $y^+ = 100$ (logarithmic layer) in M8T1.
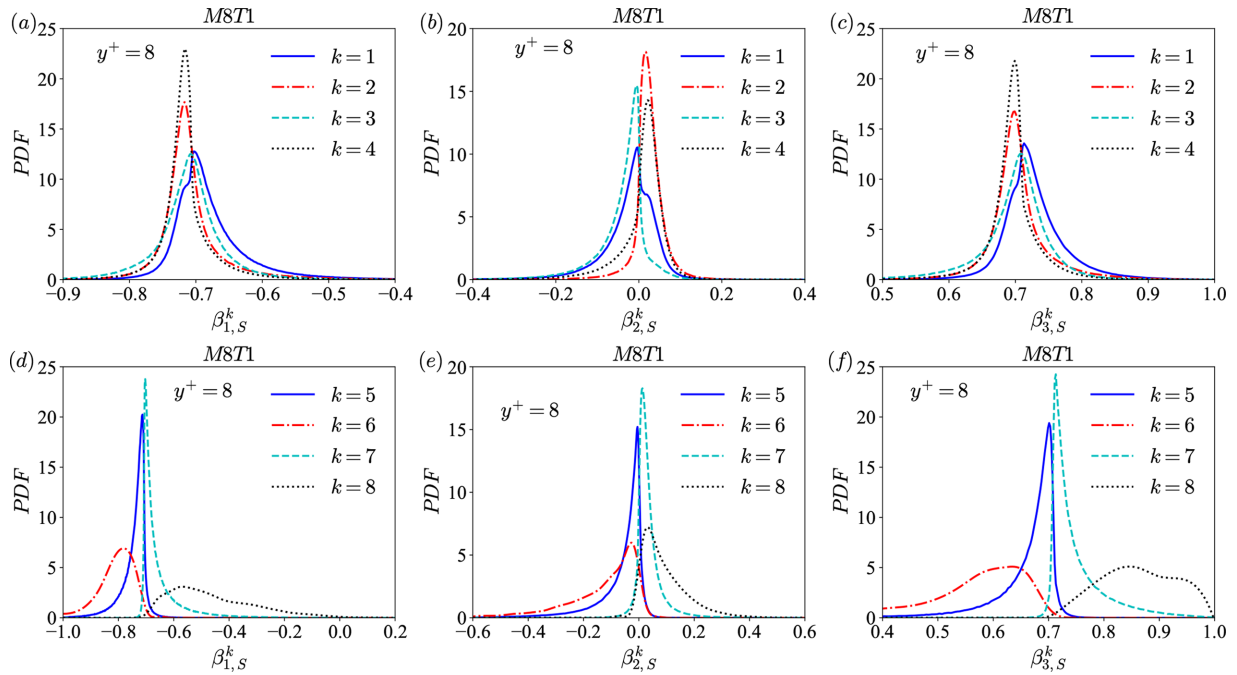
FIG. 19. (a) and (d): PDFs of the normalized eigenvalues $\beta_{1,S}$ of the strain rate tensor for different flow topologies $S^{(k)}$ at $y^+ = 8$ (buffer layer) with (a) $k = 1 - 4$ and (d) $k = 5 - 8$ in M8T1. (b) and (e): PDFs of the normalized eigenvalues $\beta_{2,S}$ of the strain rate tensor for different flow topologies $S^{(k)}$ at $y^+ = 8$ (buffer layer) with (b) $k = 1 - 4$ and (e) $k = 5 - 8$ in M8T1. (c) and (f): PDFs of the normalized eigenvalues $\beta_{3,S}$ of the strain rate tensor for different flow topologies $S^{(k)}$ at $y^+ = 8$ (buffer layer) with (c) $k = 1 - 4$ and (f) $k = 5 - 8$ in M8T1.
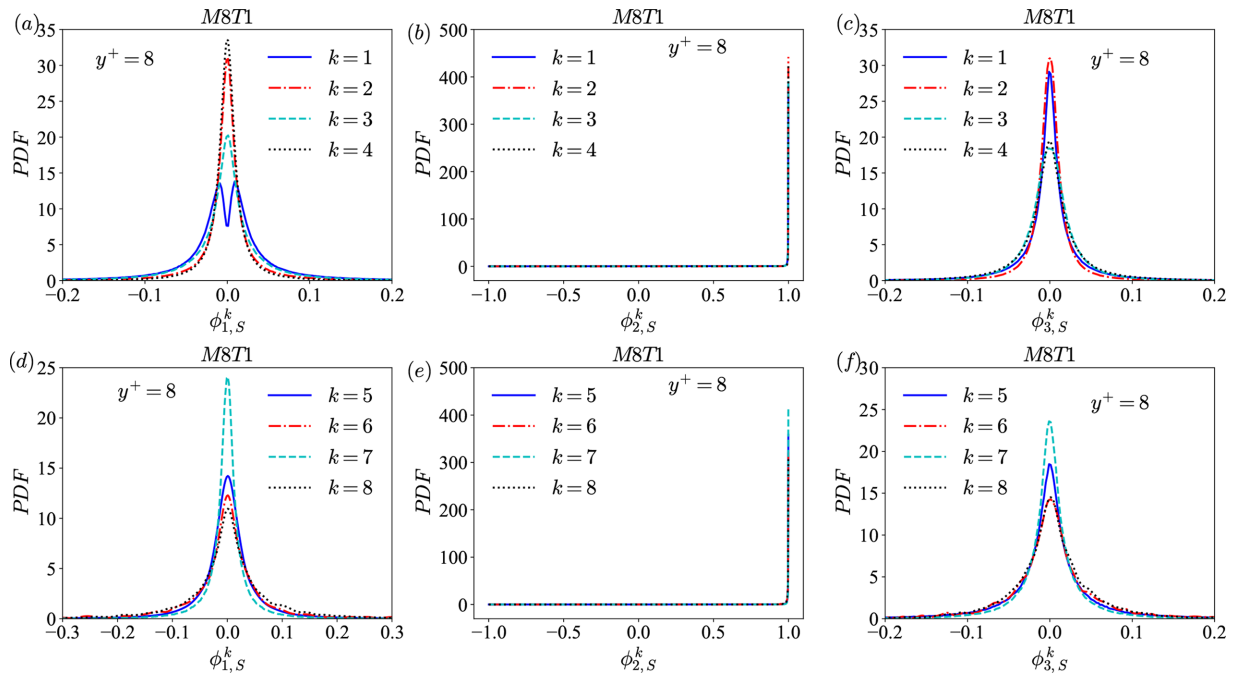

FIG. 20. (a) and (d): PDFs of the cosines of the angles between vorticity and eigenvectors $\phi_{1,S}$ for different flow topologies $S^{(k)}$ at $y^+ = 8$ (buffer layer) with (a) $k = 1 - 4$ and (d) $k = 5 - 8$ in M8T1. (b) and (e): PDFs of the cosines of the angles between vorticity and eigenvectors $\phi_{2,S}$ for different flow topologies $S^{(k)}$ at $y^+ = 8$ (buffer layer) with (b) $k = 1 - 4$ and (e) $k = 5 - 8$ in M8T1. (c) and (f): PDFs of the cosines of the angles between vorticity and eigenvectors $\phi_{3,S}$ for different flow topologies $S^{(k)}$ at $y^+ = 8$ (buffer layer) with (c) $k = 1 - 4$ and (f) $k = 5 - 8$ in M8T1.
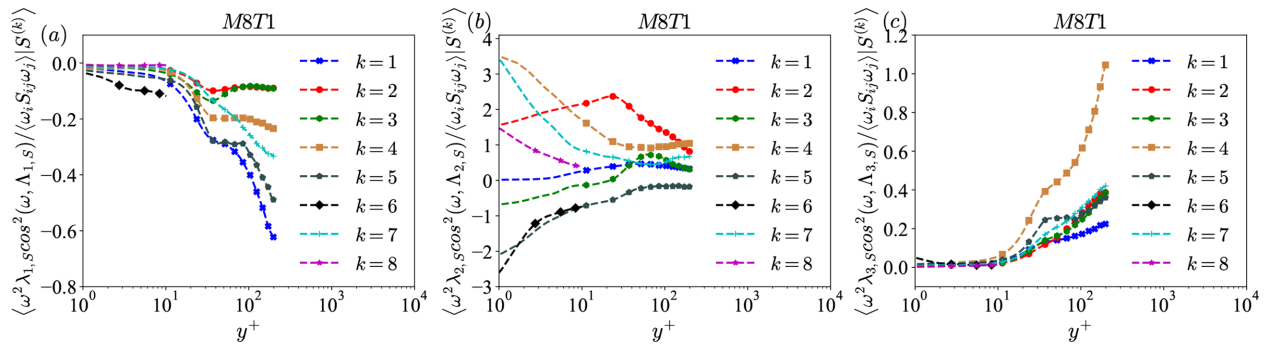
FIG. 21. The averages of the contributions of (a) the first eigenvector of the strain rate tensor $\Lambda_{1,S}$, (b) the intermediate eigenvector of the strain rate tensor $\Lambda_{2,S}$, and (c) the third eigenvector of the strain rate tensor $\Lambda_{3,S}$ to the enstrophy production conditioned on different flow topologies $S^{(k)}$ along the wall-normal direction in M8T1. It is noted that we only plot the contributions by the flow topologies $S^{(6)}$ and $S^{(8)}$ in the near-wall region, due to the almost zero volume fractions of the flow topologies $S^{(6)}$ and $S^{(8)}$ far from the wall shown in Fig. 5(a).

eigenvector is prominent in all eight flow topologies, and the alignment is slightly more remarkable for the flow topologies $S^{(2)}$, $S^{(4)}$, and $S^{(7)}$ than for other topologies, indicating that the vorticity is favorable to align with the intermediate eigenvector for the flow topologies with unstable node and stretching structures. The vorticity prefers to be perpendicular to the first eigenvector for the topologies $S^{(2)}$, $S^{(3)}$, $S^{(4)}$, and $S^{(7)}$ and has a significant tendency to be perpendicular to the third eigenvector for the topologies $S^{(1)}$, $S^{(2)}$, and $S^{(7)}$. It is suggested that the flow topologies with saddle and stretching structures induce the

perpendicular alignment between the vorticity and the first eigenvector, and the flow topologies with unstable structures induce the perpendicular alignment between the vorticity and the third eigenvector.

The averages of the contributions of the three eigenvectors of the strain rate tensor $\Lambda_{j,S}$ to the enstrophy production conditioned on different flow topologies $S^{(k)}$ along the wall-normal direction in M8T1 are shown in Fig. 21. It is found that in the near wall region, the enstrophy production is mainly contributed by the intermediate eigenvalue, which confirms the significant contribution of the intermediate
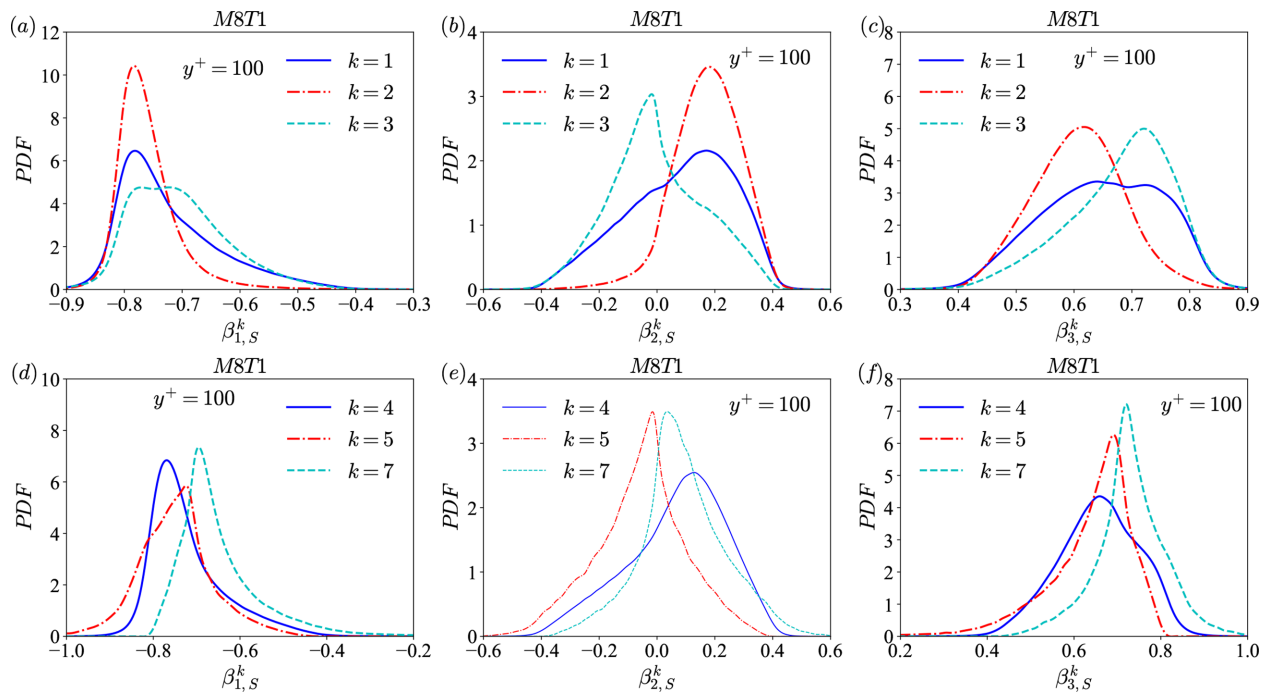

FIG. 22. (a) and (d): PDFs of the normalized eigenvalues $\beta_{1,S}$ of the strain rate tensor for different flow topologies $S^{(k)}$ at $y^+ = 100$ (logarithmic layer) with (a) $k = 1$, 2, and 3 and (d) $k = 4$, 5, and 7 in M8T1. (b) and (e): PDFs of the normalized eigenvalues $\beta_{2,S}$ of the strain rate tensor for different flow topologies $S^{(k)}$ at $y^+ = 100$ (logarithmic layer) with (b) $k = 1$, 2, and 3 and (e) $k = 4$, 5, and 7 in M8T1. (c) and (f): PDFs of the normalized eigenvalues $\beta_{3,S}$ of the strain rate tensor for different flow topologies $S^{(k)}$ at $y^+ = 100$ (logarithmic layer) with (c) $k = 1$, 2, 3 and (f) $k = 4$, 5, 7 in M8T1.
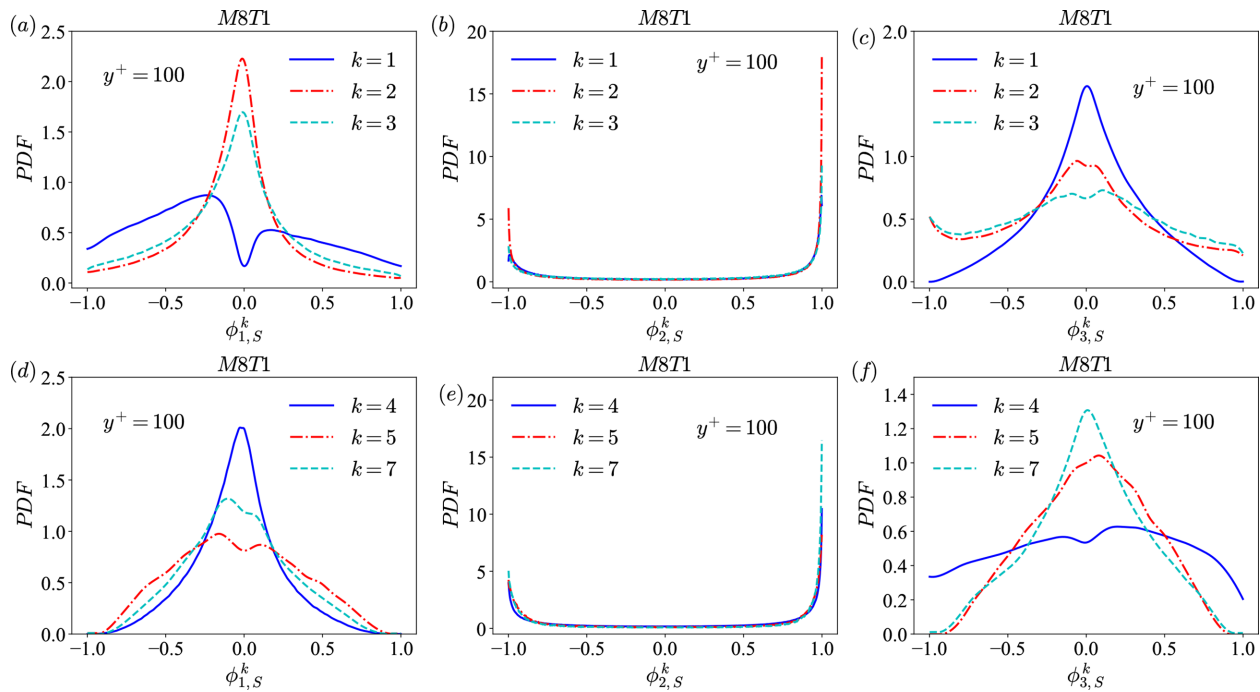
FIG. 23. (a) and (d): PDFs of the cosines of the angles between vorticity and eigenvectors $\phi_{1,S}$ for different flow topologies $S^{(k)}$ at $y^+ = 100$ (logarithmic layer) with (a) $k = 1$, 2, and 3 and (d) $k = 4$, 5, and 7 in M8T1. (b) and (e): PDFs of the cosines of the angles between vorticity and eigenvectors $\phi_{2,S}$ for different flow topologies $S^{(k)}$ at $y^+ = 100$ (logarithmic layer) with (b) $k = 1$, 2, and 3 and (e) $k = 4$, 5, and 7 in M8T1. (c) and (f): PDFs of the cosines of the angles between vorticity and eigenvectors $\phi_{3,S}$ for different flow topologies $S^{(k)}$ at $y^+ = 100$ (logarithmic layer) with (c) $k = 1$, 2, and 3 and (f) $k = 4$, 5, and 7 in M8T1.

eigenvalue $\beta_{2,S}$ to the enstrophy production.[47] Furthermore, the term $\lambda_{2,S} \cos^2(\omega, \Lambda_{2,S})$ significantly contributes to the positive enstrophy production in flow topologies $S^{(2)}$, $S^{(4)}$, $S^{(7)}$, and $S^{(8)}$, indicating that the unstable and stretching structures mainly lead to the enstrophy production. On the other hand, the term $\lambda_{2,S} \cos^2(\omega, \Lambda_{2,S})$ exhibits the enstrophy destruction in flow topologies $S^{(3)}$, $S^{(5)}$, and $S^{(6)}$, implying that the stable and compressing structures mainly give rise to the enstrophy destruction. The term $\lambda_{2,S} \cos^2(\omega, \Lambda_{2,S})$ in flow topology $S^{(1)}$, and the terms $\lambda_{1,S} \cos^2(\omega, \Lambda_{1,S})$ and $\lambda_{3,S} \cos^2(\omega, \Lambda_{3,S})$ give negligible contributions to the enstrophy production.

PDFs of the normalized eigenvalues $\beta_{j,S}$ of the strain rate tensor for the flow topologies $S^{(k)}$ at $y^+ = 100$ (logarithmic layer) are plotted in Fig. 22. The volume fractions of flow topologies $S^{(6)}$ and $S^{(8)}$ are almost zero due to weak compressibility at $y^+ = 100$; thus, PDFs of $\beta_{j,S}$ in these two flow topologies are ignored. In the logarithmic layer, the shape of PDF of $\beta_{2,S}$ in the flow topology $S^{(1)}$ is wide, which has the positive value of peak location. The most probable values of $\beta_{2,S}$ in flow topologies $S^{(2)}$, $S^{(4)}$, and $S^{(7)}$ are positive, while the peak locations of $\beta_{2,S}$ in flow topologies $S^{(3)}$ and $S^{(5)}$ are negative.

PDFs of the cosines of the angle between vorticity and eigenvectors $\phi_{j,S_{ij}}$ for the flow topologies $S^{(k)}$ at $y^+ = 100$ (logarithmic layer) are plotted in Fig. 23. In the logarithmic layer, the alignment between the vorticity and the intermediate eigenvector is more significant for the topologies $S^{(2)}$, $S^{(4)}$, and $S^{(7)}$ than for other topologies, which is similar to the observation in the buffer layer. Furthermore, the vorticity has a significant tendency to be perpendicular to the first

eigenvector for the topologies $S^{(2)}$, $S^{(3)}$, and $S^{(4)}$, and prefers to be perpendicular to the third eigenvector for the topologies $S^{(1)}$, $S^{(5)}$, and $S^{(7)}$. Accordingly, it is indicated that the flow topologies with saddle and stretching structures induce the perpendicular alignment between the vorticity and the first eigenvector, and the flow topologies with unstable focus and compressing structures induce the perpendicular alignment between the vorticity and the third eigenvector.

It is shown in Fig. 21 that all three eigenvalues $\beta_{j,S}$ of the strain rate tensor contribute significantly to the enstrophy production from the wall. The term $\lambda_{1,S} \cos^2(\omega, \Lambda_{1,S})$ leads to the enstrophy destruction, especially in flow topologies $S^{(1)}$ and $S^{(5)}$. This observation implies that the compressing structures mainly give rise to the enstrophy destruction through the first eigenvalue far from the wall. The term $\lambda_{3,S} \cos^2(\omega, \Lambda_{3,S})$ gives rise to the enstrophy production, especially in flow topology $S^{(4)}$. This finding indicates that the compressive vortical structures with an out-of-plane stretching strain result in the enstrophy production through the third eigenvalue far from the wall. The term $\lambda_{2,S} \cos^2(\omega, \Lambda_{2,S})$ has significant contribution to both the enstrophy production and destruction. The flow topology $S^{(5)}$ leads to the enstrophy destruction, while other five flow topologies results in the enstrophy production in term $\lambda_{2,S} \cos^2(\omega, \Lambda_{2,S})$, especially in flow topology $S^{(2)}$. This suggests that the compressive vortical structures with an out-of-plane compressing strain lead to the enstrophy destruction through the intermediate eigenvalue far from the wall.

V. SUMMARY AND CONCLUSION

In this paper, the statistical properties of the small-scale structures and flow topologies in the hypersonic turbulent boundary layer with an isothermal wall condition are investigated. The effects of local compressibility, wall temperature, and various flow topologies on the enstrophy production as well as the eigenvalues and eigenvectors of the strain rate tensor are studied. The Helmholtz decomposition is employed to investigate the effect of compressibility on the solenoidal and dilatational components of the enstrophy production.

Investigations of volume fractions of various flow topologies across the boundary layer indicate that the influence of wall temperature on flow patterns is concentrated on the near wall region. The observations imply that the flow is favorable to be expansive and unstable, and the colder wall temperature significantly enhances the unstable topologies near the wall. Furthermore, the focal topologies and the vortical structures are dominant across the boundary layer, and the colder wall temperature drastically decreases the volume fractions of the focal topologies in the near wall region, mainly due to the generation of more sheet-like structures. Conditional volume fractions show that the percentages of SN/S/S, SFC, and SN/SN/SN increase, while those of UFC, UN/S/S, and SFS decrease as the magnitude of the fluctuating velocity divergence increases in the compression region. Moreover, volume fractions of UFS and UN/UN/UN increase, while those of UFC, UN/S/S, SN/S/S, and SFS decrease as the fluctuating velocity divergence becomes larger in the expansion region. SN/S/S and SFC play the major role in the strong compression region, while UFS predominates in the strong expansion region.

The eigenvalue decomposition of the strain rate tensor is helpful to investigate the mechanism of the enstrophy production and small-scale structures. There is a strong tendency for the vorticity to align with the intermediate eigenvector and be perpendicular to the first and third eigenvectors in the buffer layer mainly due to the strong wall effect. However, in the logarithmic layer, the tendency for the vorticity to align with the intermediate eigenvector and be perpendicular to the first eigenvector becomes weaker, and the distribution of the angle between the vorticity and the third eigenvector becomes approximately uniform. Moreover, the enstrophy production is primarily contributed by the intermediate eigenvalue, while the contributions of the first and third eigenvalues are negligible near the wall. As the wall-normal distance increases, both the intermediate and third eigenvalues have the strong contributions to the enstrophy production, and the first eigenvalue plays the dominant role in the enstrophy destruction.

Various flow topologies exhibit different effects on the enstrophy production by the interaction between the vorticity and strain rate tensor. In the near wall region, the term $\lambda_{2,S}\cos^2(\omega, \Lambda_{2,S})$ in flow topologies UN/S/S, SFS, UFS, and UN/UN/UN gives the significant contribution to the enstrophy production, while the term $\lambda_{2,S}\cos^2(\omega, \Lambda_{2,S})$ in flow topologies SN/S/S, SFC, and SN/SN/SN contributes to the enstrophy destruction. Moreover, in the far wall region, $\lambda_{1,S}\cos^2(\omega, \Lambda_{1,S})$ in flow topologies UFC and SFC, and $\lambda_{2,S}\cos^2(\omega, \Lambda_{2,S})$ in flow topology SFC lead to the enstrophy destruction, while $\lambda_{3,S}\cos^2(\omega, \Lambda_{3,S})$ in flow topology SFS and $\lambda_{2,S}\cos^2(\omega, \Lambda_{2,S})$ flow topology UN/S/S give rise to the enstrophy production.

In this study, the effects of local compressibility, wall temperature, and local flow topology on the small-scale motions in the hypersonic turbulent boundary layer are investigated. These new observations give guidance to understand the properties and mechanisms of the small-scale motions in the hypersonic turbulent boundary layer. However, the statistics and dynamics of the local topological evolution and the relevant Lagrangian models aiming to study the characteristics of coherent structures are not included in this paper, which are left for future studies.

AUTHOR DECLARATIONS

Conflict of Interest

The authors have no conflicts to disclose.

DATA AVAILABILITY

The data that support the findings of this study are available from the corresponding author upon reasonable request.

APPENDIX: GRID CONVERGENCE OF THE DATABASES

The grid resolutions of the present databases are assessed by the grid convergence studies. It is noted that $\widetilde{f} = \overline{\rho f}/\overline{\rho}$ represents the Favre average of f, and the fluctuating counterpart is $f'' = f - \widetilde{f}$. The normalized streamwise Reynolds stress $\langle \rho u''^2 \rangle / \tau_w$ and the normalized r.m.s. values of fluctuating temperature $\sqrt{\langle T''^2 \rangle}/T_w$ with four different grid resolutions listed in Table IV in M8T2 are shown in Fig. 24. It is noted that the symbol "$\langle f \rangle$" represents the Reynolds average (spanwise and time average) of the variable f. It is seen that all the curves collapse indistinguishably, indicating that the grid resolution "A" is sufficient to resolve both the turbulent and thermal boundary layers in M8T2. Furthermore, the grid resolution in M8T1 is finer than that in M8T2, and the grid convergence is also checked in M8T1, which is omitted for brevity.

TABLE IV. Four different grid resolutions used for the grid convergence studies in M8T2.

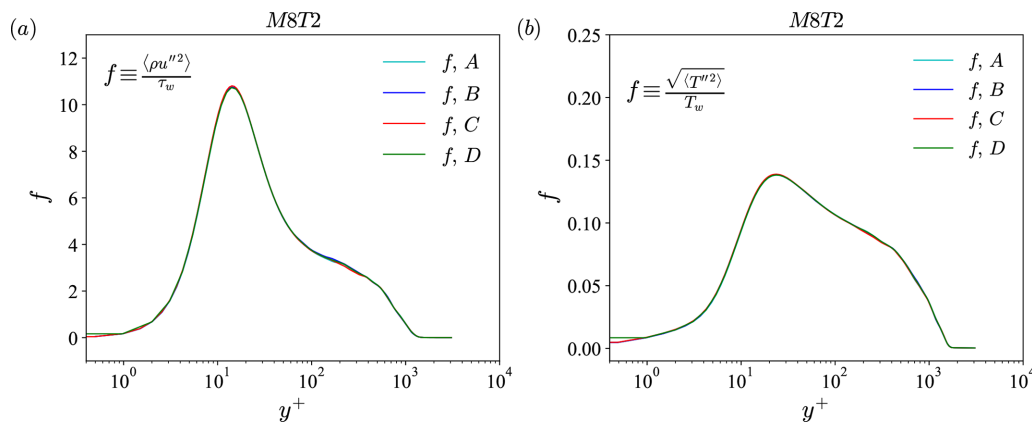| Case	$N_x \times N_y \times N_z$	Δx^+	Δy_w^+	Δz^+
M8T2-A	$12500 \times 200 \times 640$	12.2	0.5	4.6
M8T2-B	$12500 \times 200 \times 1280$	12.2	0.5	2.3
M8T2-C	$25000 \times 200 \times 640$	6.1	0.5	4.6
M8T2-D	$12500 \times 100 \times 640$	12.2	1.0	4.6

FIG. 24. Grid convergence study for M8T2. (a) The normalized streamwise Reynolds stress $\langle \rho u''^2 \rangle / \tau_w$ with four different grid resolutions. (b) The normalized r.m.s. values of fluctuating temperature $\sqrt{\langle T''^2 \rangle}/T_w$ with four different grid resolutions. The symbols "A," "B," "C," and "D" represent four different grid resolutions and are listed in Table IV. The grid resolution "A" is the resolution used for further analysis in M8T2.

REFERENCES

[1]A. J. Smits and J. P. Dussauge, *Turbulent Shear Layers in Supersonic Flow* (Springer, 2006).

[2]T. Cebeci and A. M. O. Smith, *Analysis of Turbulent Boundary Layers* (Academic, 1974).

[3]T. B. Gatski and J. P. Bonnet, *Compressibility, Turbulence and High Speed Flow* (Elsevier, 2009).

[4]L. Duan, I. Beekman, and M. P. Martin, "Direct numerical simulation of hypersonic turbulent boundary layers. Part 2. Effect of wall temperature," J. Fluid Mech. **655**, 419–445 (2010).

[5]L. Duan, I. Beekman, and M. P. Martin, "Direct numerical simulation of hypersonic turbulent boundary layers. Part 3. Effect of Mach number," J. Fluid Mech. **672**, 245–267 (2011).

[6]M. Lagha, J. Kim, J. D. Eldredge, and X. Zhong, "A numerical study of compressible turbulent boundary layers," Phys. Fluids **23**, 015106 (2011).

[7]S. Pirozzoli, F. Grasso, and T. B. Gatski, "Direct numerical simulation and analysis of a spatially evolving supersonic turbulent boundary layer at M = 2.25," Phys. Fluids **16**, 530–545 (2004).

[8]S. Pirozzoli, M. Bernardini, and F. Grasso, "On the dynamical relevance of coherent vortical structures in turbulent boundary layers," J. Fluid Mech. **648**, 325–349 (2010).

[9]J. Tang, Z. Zhao, Z. Wan, and N. Liu, "On the near-wall structures and statistics of fluctuating pressure in compressible turbulent channel flows," Phys. Fluids **32**, 115121 (2020).

[10]F. Tong, S. Dong, J. Lai, X. Yuan, and X. Li, "Wall shear stress and wall heat flux in a supersonic turbulent boundary layer," Phys. Fluids **34**, 015127 (2022).

[11]X. Liang and X. Li, "DNS of a spatially evolving hypersonic turbulent boundary layer at Mach 8," Sci. China **56**, 1408–1418 (2013).

[12]Y. Chu, Y. Zhuang, and X. Lu, "Effect of wall temperature on hypersonic turbulent boundary layer," J. Turbul. **14**, 37–57 (2013).

[13]J. M. Wallace, "Twenty years of experimental and direct numerical simulation access to the velocity gradient tensor: What have we learned about turbulence?," Phys. Fluids **21**, 021301 (2009).

[14]C. Meneveau, "Lagrangian dynamics and models of the velocity gradient tensor in turbulent flows," Annu. Rev. Fluid Mech. **43**, 219–245 (2011).

[15]M. S. Chong, A. E. Perry, and B. J. Cantwell, "A general classification of three-dimensional flow fields," Phys. Fluids A **2**, 765–777 (1990).

[16]H. M. Blackburn, N. N. Mansour, and B. J. Cantwell, "Topology of fine scale motions in turbulent channel flow," J. Fluid Mech. **310**, 269–292 (1996).

[17]M. S. Chong, J. Soria, A. E. Perry, J. Chacin, B. J. Cantwell, and Y. Na, "Turbulence structures of wall bounded shear flows found using DNS data," J. Fluid Mech. **357**, 225–247 (1998).

[18]G. E. Elsinga and I. Marusic, "Universal aspects of small-scale motions in turbulence," J. Fluid Mech. **662**, 514–539 (2010).

[19]A. Lozano-Durán, A. Holzner, and J. Jiménez, "Multiscale analysis of the topological invariants in the logarithmic region of turbulent channels at a friction Reynolds number of 932," J. Fluid Mech. **803**, 356–394 (2016).

[20]Y. Chen, X. Wang, Z. Jiang, and J. Wang, "Effect of heat source on statistics and scaling in compressible homogeneous shear turbulence," Phys. Fluids **33**, 125128 (2021).

[21]L. Duan, Q. Zheng, Z. Jiang, and J. Wang, "Dense gas effect on small-scale structures of compressible isotropic turbulence," Phys. Fluids **33**, 115113 (2021).

[22]S. Suman and S. S. Girimaji, "Velocity gradient invariants and local flow-field topology in compressible turbulence," J. Turbul. **11**, 1–24 (2010).

[23]J. Wang, Y. Shi, L. Wang, Z. Xiao, X. He, and S. Chen, "Effect of compressibility on the small-scale structures in isotropic turbulence," J. Fluid Mech. **713**, 588–631 (2012).

[24]J. Wang, M. Wan, S. Chen, C. Xie, Q. Zheng, L. Wang, and S. Chen, "Effect of flow topology on the kinetic energy flux in compressible isotropic turbulence," J. Fluid Mech. **883**, A11 (2020).

[25]X. Wang, S. Chen, J. Wang, H. Li, M. Wan, and S. Chen, "Effect of compressibility on the local flow topology in homogeneous shear turbulence," Phys. Fluids **32**, 015118 (2020).

[26]D. Xu, J. Wang, C. Yu, X. Li, and S. Chen, "Contribution of flow topology to the kinetic energy flux in hypersonic turbulent boundary layer," Phys. Fluids **34**, 046103 (2022).

[27]M. Danish, S. Suman, and S. S. Girimaji, "Influence of flow topology and dilatation on scalar mixing in compressible turbulence," J. Fluid Mech. **793**, 633–655 (2016).

[28]L. Wang and X. Lu, "Flow topology in compressible turbulent boundary layer," J. Fluid Mech. **703**, 255–278 (2012).

[29]Y. Chu and X. Lu, "Topological evolution in compressible turbulent boundary layers," J. Fluid Mech. **733**, 414–438 (2013).

[30]P. Bechlars and R. D. Sandberg, "Variation of enstrophy production and strain rotation relation in a turbulent boundary layer," J. Fluid Mech. **812**, 321–348 (2017).

[31]P. Bechlars and R. D. Sandberg, "Evolution of the velocity gradient tensor invariant dynamics in a turbulent boundary layer," J. Fluid Mech. **815**, 223–242 (2017).

[32]D. Xu, J. Wang, M. Wan, C. Yu, X. Li, and S. Chen, "Compressibility effect in hypersonic boundary layer with isothermal wall condition," Phys. Rev. Fluids **6**, 054609 (2021).

[33]D. Xu, J. Wang, M. Wan, C. Yu, X. Li, and S. Chen, "Effect of wall temperature on the kinetic energy transfer in hypersonic turbulent boundary layer," J. Fluid Mech. **929**, A33 (2021).

[34]D. Xu, J. Wang, and S. Chen, "Skin friction and heat transfer in hypersonic transitional and turbulent boundary layers," J. Fluid Mech. **941**, A4 (2022).

[35]D. S. Balsara and C. Shu, "Monotonicity preserving weighted essentially non-oscillatory schemes with increasingly high order of accuracy," J. Comput. Phys. **160**, 405–452 (2000).

[36]G. Hirasaki and J. Hellums, "Boundary conditions on the vector and scalar potentials in viscous three-dimensional hydrodynamics," Q. Appl. Math. **28**, 293–296 (1970).

[37]M. Yu, C. Xu, and S. Pirozzoli, "Genuine compressibility effects in wall-bounded turbulence," Phys. Rev. Fluids **4**, 123402 (2019).

[38]M. Yu, C.-X. Xu, and S. Pirozzoli, "Compressibility effects on pressure fluctuation in compressible turbulent channel flows," Phys. Rev. Fluids **5**, 113401 (2020).

[39]M. Yu and C. Xu, "Compressibility effects on hypersonic turbulent channel flow with cold walls," Phys. Fluids **33**, 075106 (2021).

[40]J. Soria, R. Sondergaard, B. J. Cantwell, M. S. Chong, and A. E. Perry, "A study of the fine-scale motions of incompressible time-developing mixing layers," Phys. Fluids **6**, 871–884 (1994).

[41]S. Pirozzoli and F. Grasso, "Direct numerical simulations of isotropic compressible turbulence: Influence of compressibility on dynamics and structures," Phys. Fluids **16**, 4386–4407 (2004).

[42]W. T. Ashurst, A. R. Kerstein, R. M. Kerr, and C. H. Gibson, "Alignment of voticity and scalar gradient with strain rate in simulated Navier-Stokes turbulence," Phys. Fluids **30**, 2343–2353 (1987).

[43]G. Erlebacher and S. Sarkar, "Statistical analysis of the rate of strain tensor in compressible homogeneous turbulence," Phys. Fluids A **5**, 3240–3254 (1993).

[44]A. A. Townsend, *The Structure of Turbulent Shear Flow* (Cambridge University Press, 1976).

[45]B. Galanti and A. Tsinober, "Self-amplification of the field of velocity derivatives in quasi-isotropic turbulence," Phys. Fluids **12**, 3097–3099 (2000).

[46]M. Kholmyansky, A. Tsinober, and S. Yorish, "Velocity derivatives in the atmospheric surface layer at $Re_\lambda = 10^4$," Phys. Fluids **13**, 311–314 (2001).

[47]R. Betchov, "An inequality concerning the production of vorticity in isotropic turbulence," J. Fluid Mech. **1**, 497–504 (1956).